2019

Effects of Lubrication Starvation on Flash Temperature for Thermal Mixed Elastohydrodynamic Gear Contacts

Danielle D. Massé
Wright State University

Effects of Lubrication Starvation on Flash Temperature for Thermal Mixed Elastohydrodynamic Gear Contacts

A thesis submitted in partial fulfillment
of the requirements for the degree of
Master of Science in Mechanical Engineering

by

DANIELLE D. MASSÉ
B.S., College of Charleston, 2016

2019
Wright State University

Wright State University
GRADUATE SCHOOL

November 21, 2019

I HEREBY RECOMMEND THAT THE THESIS PREPARED UNDER MY SUPERVISION BY Danielle D. Massé ENTITLED Effects of Lubrication Starvation on Flash Temperature for Thermal Mixed Elastohydrodynamic Gear Contacts BE ACCEPTED IN PARTIAL FULFILLMENT OF THE REQUIREMENTS FOR THE DEGREE OF Master of Science in Mechanical Engineering.

Sheng Li, Ph.D.
Thesis Director

Raghavan Srinivasan, Ph.D., P.E.
Interim Chair, Department of Mechanical and Materials Engineering

Committee on
Final Examination

Sheng Li, Ph.D.

Ahsan Mian, Ph.D.

Harok Bae, Ph.D.

Barry Milligan, Ph.D.
Interim Dean of the Graduate School

ABSTRACT

Massé, Danielle D. M.S.M.E., Department of Mechanical and Materials Engineering, Wright State University, 2019. *Effects of Lubrication Starvation on Flash Temperature for Thermal Mixed Elastohydrodynamic Gear Contacts.*

Lubrication is provided to the gear trains in automotive and aerospace transmission systems to prevent mechanical contact through the formation of a full lubricant film, which in turn removes heat generated at the gear contact surfaces. When debris blocks the inlet nozzle, the flow of lubricant is restricted and mechanical components experience lubrication starvation. Under starved lubrication the temperatures of the contact surfaces become elevated which can lead to the formation of a weld between them, a catastrophic failure mode called scuffing. For spur gears, the occurrence of scuffing is due to high sliding in the vicinity of the root or tip, where the shear thinning effect decreases the lubrication film thickness. This lubricant depletion increases the contact pressure and frictional heat flux beyond a critical limit, resulting in weld formation. The weld is immediately torn apart by the continuous relative motion of the components, causing extreme damage to the tooth surfaces. The objective of this study is to characterize the tribological behavior of high sliding gear contacts under starved lubrication. This is achieved through numerical flow simulations which utilize a generalized Reynolds equation with a non-Newtonian flow coefficient, and incorporate the dependence of lubricant viscosity on pressure and temperature. In order to study the effects of lubrication starvation a film fraction parameter is used in the Reynolds equation, removing the need for measured or assumed inlet lubrication geometry. This work presents a parametric study of engineering surface profiles under different operating conditions to show an asymptotic relationship between flash temperature and the severity of the lubrication starvation, supported by an analysis of pressure, film fraction parameter, friction coefficient, and power loss. The results of these investigations justify further numerical and experimental studies of scuffing failure for gear contacts.

List of Symbols

a_h	Hertzian half width
A_s	surface area of differential area element
c_f	specific heat of the lubricant
E'	reduced elastic modulus of the mating surfaces
f	friction force
g_{in}	gap between the solid surfaces in the inlet zone
h	film thickness
h_1^{in}, h_2^{in}	height of lubricant attached to surfaces 1 and 2 respectively
h_{in}	inlet film thickness, found as $h_{in} = h_1^{in} + h_2^{in}$
h_0	rigid body approach of the bounding surfaces
h_m	average film thickness within the nominal Hertzian zone
$\bar{h}_m^{fld}$	median average film thickness under fully flood lubrication condition
k_f	thermal conductivity of the lubricant
k_s	thermal conductivity of the solid surface
p	pressure
p^{max}	maximum contact pressure
$\bar{p}^{\,max}$	median maximum contact pressure
p_h	Hertzian pressure
$\hat{p}_x$	dimensionless pressure gradient
P	power loss
Q	total heat flux
Q_1, Q_2	heat flux of surfaces 1 and 2 respectively
R'	reduced radius of curvature of the mating surfaces
R_q	root mean square roughness amplitude
R_q^c	composite root mean square roughness amplitude

SR	slide-to-roll ratio $SR = \frac{u_s}{u_r}$
T_f	temperature
T_m	mean temperature
T_{in}	inlet lubricant temperature
T_{lub}	lubricant temperature
T_1, T_2	temperature of surfaces 1 and 2 respectively
T_1^b, T_2^b	bulk temperature of surfaces 1 and 2 respectively
${T_1}^{max}, {T_2}^{max}$	maximum temperature of surfaces 1 and 2 respectively
$\bar{T_1}^{max}, \bar{T_2}^{max}$	median maximum temperature of surfaces 1 and 2 respectively
$\triangle T_1, \triangle T_2$	flash temperature rise of surfaces 1 and 2 respectively
t	time
θ	fluid film fraction parameter
θ_{in}	film fraction boundary condition
u_1, u_2	velocities of surfaces 1 and 2 respectively in the direction of rolling
u_r	rolling velocity $u_r = \frac{u_1+u_2}{2}$
u_s	sliding velocity $u_s = u_1 - u_2$
V	elastic deformation
W	applied load
x	coordinate along the rolling direction
z	coordinate perpendicular to the rolling direction
$\hat{z}$	dimensionless coordinate perpendicular to the rolling direction
η	low-shear viscosity of the lubricant
ν	lubricant viscosity
ρ	lubricant density
ρ_0	fluid density under ambient pressure and temperature
λ_1, λ_2	constants associated with density compressibility
λ_3	thermal expansion coefficient associated with $\triangle T_f$

ϑ	heat partition coefficient
κ_s	thermal diffusivity of the solid surface
ϕ	flow coefficient
τ	shear stress
$\hat{\tau}$	dimensionless shear stress
$\dot{\gamma}$	shear strain rate
χ_W	ratio of force supported by asperity contacts to total normal force

Contents

List of Figures

List of Tables

Acknowledgment

First and foremost, I want to thank the students and faculty from the Mathematics and Mechanical and Materials engineering departments for their support in navigating the crooked path that I have followed in graduate school. Without them, it is likely that I never would have found my place in the world as an engineer.

The research supporting this thesis would not be possible without the expertise and capabilities of Dr. Sheng Li. As any advisor does, he took a chance welcoming me into his lab and for that I am very grateful. Our discussions have inspired many useful ideas and helped me grow as a researcher.

Dedicated to Anne Michau, who exemplified perseverance and kindness in all things.

Additionally, I want to thank my parents, Beth and Gaétan Massé, for their encouragement and support which made all of my ambitions a reality.

Introduction

1.1 Background and Motivation

First established by an analysis presented by Heinrich Hertz in 1881, contact mechanics is the study of the deformation of solids that make contact with each other. Since Hertz, much progress has been made in the field of tribology concerning the design, performance, production, and reliability of countless tribosystems. A tribosystem is a mechanical system containing one or more triboelements, or solid bodies coming into contact with each other via sliding, rolling, or abrasive contact [1]. The two portions of the triboelements which make contact are typically referred to as the mating surfaces, or contact surfaces. Today, many researchers in engineering and materials science focus on the microscopic asperity interactions that occur on contact surfaces, with particular interest in expanding the understanding of known failure modes and how they relate to operating and lubrication conditions. Before delving into the problem this work addresses, it is first necessary to understand the fundamentals of lubrication and contact theory for generalized tribosystems.

1.1.1 Hertzian Contact Theory

In general, when any two curved surface with different radii of curvature are brought into contact, they will touch at either a point or along a line. When a load is applied, elastic deformation of the surfaces enlarges the initial point/line into a contact area across which

the load is distributed as pressure. In classical contact mechanics, the two solids coming into contact and deforming are assumed to be isotropic and homogeneous [2]. As defined by Bhushan et al. in [2], Hertzian theory is a subset of contact mechanics which further assumes that:

i) The surfaces are continuous, smooth, nonconforming, and frictionless

ii) The size of the contact area is small compared to the size of the bodies, i.e., the strains associated with the deformations are small

iii) Each solid can be considered to behave as an elastic half-space in the vicinity of the contact zone

iv) The gap h between the undeformed surfaces can be approximated by an expression of the form $h = Ax^2 + By^2$ where x and y are orthogonal coordinates lying in the common tangent plane to the two surfaces

Hence, by assumption iv), Hertzian theory is applicable to the contact of spheres, cylinders, and ellipsoids. Many mechanical components have such surface profiles including several types of bearings and gears, and the types of contact can be separated into point contact (sphere on sphere) or line contact (cylinder on cylinder). As expounded in detail in 1.1.4, the contact made between involute spur gears is a line contact. To properly motivate the modern areas of study for gear contacts, it is necessary to discuss the failure modes that such a line contact under high load and relative velocities can experience.

1.1.2 Failure Modes of Tribosystems

Tribosystems can be subject to many types of failure related to the friction, lubrication, and wear conditions of the triboelements which comprise them [2–5]. The most common failure modes are fatigue, wear, and scuffing. Fatigue failures, such as bending, pitting, and micropitting, are characterized as physical failures of the contact surface or larger

mechanical component due to excessive, repeated loading and stress. Wear failure can be defined as the gradual removal of material from a surface due to interaction with a mating surface [2]. This work concerns spur gears under high speed and high sliding operating conditions which are characterized by their susceptibility to scuffing failure, and so focus will be placed on this failure mode.

Scuffing

Scuffing, also referred to as scoring or pressure-induced welding, is a failure mode frequently observed in automotive and aerospace gearing applications which is characterized by the roughening of the contact surfaces resulting from solid state weld formation. As opposed to wear, scuffing roughens contact surfaces without any net loss of material. It occurs when asperity contact is made under inadequate lubriction conditions, which leads to extreme friction between the mating surfaces - under high loads, this friction generates heat increasing the surface bulk temperature as the heat cannot be effectively removed by lubrication. The increased surface bulk temperature and high contact pressure causes solid welding of the contact surfaces. During successive rotations, the weld is broken and can result in rough contact surfaces which continue to deplete the lubricant film thus continuing the amount and severity of surface roughness. At the microscopic level, the metallic bonding necessary to form the weld occurs in three stages:

1. Asperities on the contact surfaces deform and interlink, causing interfaces between the contact surfaces.

2. Elevated temperature and pressure cause accelerated creep - grain boundaries degrade and gaps between contact surfaces are reduced to isolated pores.

3. Material diffuses across boundaries of adjacent surfaces, eliminating the boundary and creating a bond.

Scuffing occurs non-uniformly - in particular, it can spread across a contact surface over many cycles of operation. If the clearance between contact surfaces is small such that the weld cannot be broken, scuffing failure can lead to seizure. Scuffing damage to a contact surface can be visualized with a scanning electron microscopes, but it is difficult to quantify. Scuffing failure is also catastrophic - once scuffing has occurred, the contacts quickly fail as damage increases on successive cycles of operation. Hence, the capability to realistically model the conditions which can cause scuffing in order to better understand its' causes and predict when it may occur is crucial to successful tribosystem design. One of the most important factors necessary to understand failure in any tribosystem is lubrication.

1.1.3 The Role of Lubrication in Tribosystems

In the most general sense, lubrication is used to reduce friction and wear between contact surfaces in a tribosystem. The level of protection that a lubricant layer provides to the contact surfaces depends on the regime it operates under [2]. For contact surfaces in motion, the fundamental lubrication regimes are:

- Full-film/Hydrodynamic (HL): the contact surfaces are completely separated by a full, unbroken film of lubricant.
- Elastohydrodynamic (EHL): particularly for nonconforming surfaces or surfaces under high loads, this regime is governed by a sudden reduction of lubricant film thickness which causes an increase in the lubricant viscosity. When the lubricant film becomes rigid, it causes temporary elastic deformation of the contact surfaces. This deformation considerably alters the characteristics of the separating lubricant film.
- Mixed: denotes the transition region from hydrodynamic or elastohydrodynamic lubrication to boundary lubrication, where there is a mixture of asperity interaction and lubrication separation between the contact surfaces

– Boundary: the contact surfaces are close enough that substantial metal-to-metal contact of opposing asperities occurs.

Ideally, the boundary lubrication regime is wholly avoided so contact surfaces are always separated by lubricant, preventing asperity contact. In actuality, the lubricant layer can fail.

Lubrication Starvation

When not enough of the correct lubricant is supplied to a tribosystem, this is called lubrication starvation. The exact means of starvation can vary between applications and the machinery involved. For gear contacts, the most common mode of lubrication starvation is called inlet starvation, which occurs when the flow of lubricant into the contact is restricted by some blockage or contaminant in the inlet. This is the mode of starvation that the results presented here pertain to since the implemented model allowed for the percentage of blockage to be prescribed via a cavitation boundary condition. Hence, the results presented here show how the behavior of line contacts changes as the severity of the inlet starvation is increased.

1.1.4 Geometry of Involute Spur Gears in Mesh

With the understanding of Hertzian theory and the role of lubrication, it is now necessary to consider the features of spur gears that would allow two meshed gears to be modeled as a Hertzian line contact. The major components of spur gear geometry are shown in Figure 1.1, followed by Figure 1.2 which shows how some of these components relate to a pair of spur gears in mesh [6]. The teeth of spur gears most commonly have an involute profile. This profile dictates the area of the tooth which will make contact when in mesh, as shown in Figure 1.1 by the start and end of the active profile. This active profile is traced out by the point of contact when two gears are in mesh. At every point of contact, the tooth surfaces are touching along a line with length equal to the face width. The pinion is the one

of the pair with fewer teeth which drives the motion, and the gear is larger and is driven by the force applied to its teeth by the teeth of the pinion. The force that is applied by the pinion tooth on the gear tooth is applied along the line of action. Due to the involute tooth profile, the line of action always passes through the point of contact and is tangent to the base circles of both the pinion and the gear. Since gears are generally made of isotropic, homogeneous materials and their contact occurs along a line, it can be modelled as a Hertzian line contact and characterized by all of the properties presented in 2.1.

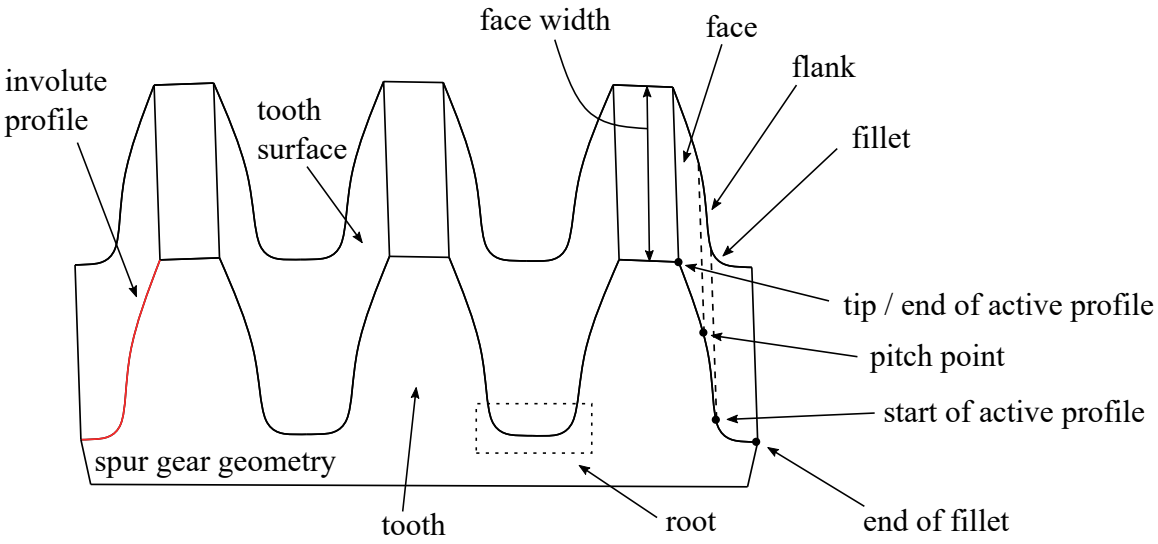

Figure 1.1: Major components of involute spur gear geometry.

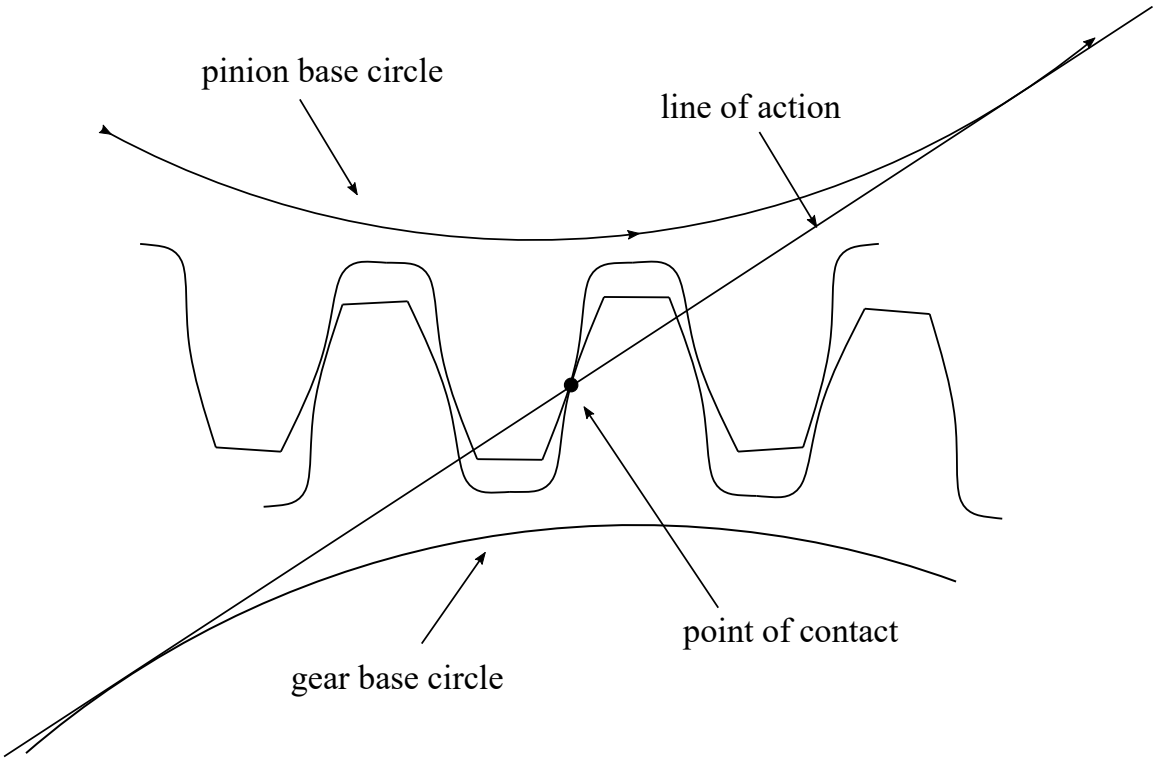

Figure 1.2: Geometry of involute spur gear pair in mesh.

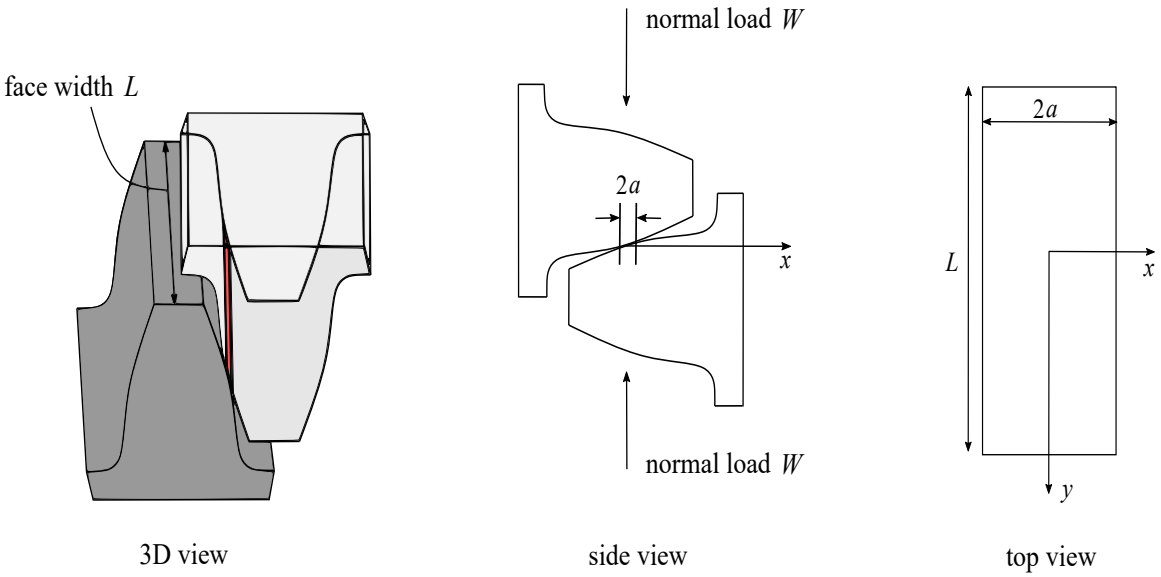

Figure 1.3: Line contact for involute spur gears.

1.2 Literature Review

Considering that scuffing failure is so catastrophic and undesirable, much research has been done on a macroscopic scale to determine the operating conditions under which it occurs, establishing some limits on operating and geometric parameters which have yielded successful gear train designs for a vast variety of applications. However, there is a much smaller subset of work which has actually focused on the physical causes of scuffing failure. Of these, relevant publications can be split into theoretical, experimental, and computational studies which focus on developing models to predict flash temperature and quantify the effects of starved lubrication.

The first well-known effort to understand and characterize scuffing failure theoretically was undertaken by Blok [7]. He proposed that scuffing occurred when a critical maximum temperature was reached in the contact area between two sliding bodies. This critical temperature was the sum of the bulk surface temperature and the instantaneous, i.e. flash, temperature rise that occurs along an EHL contact. As a result of his assumptions, Blok's model is valid for smooth, ideal surfaces and requires sufficient operation time to allow the temperature distribution to reach its steady state. In [8], Dyson's model suggests that scuffing occurs due to EHL film breakdown. This breakdown is due to a sudden decrease in the lubricant viscosity caused by frictional heating generated at a critical temperature, and causes the majority of the load to be transferred from the lubricant to the asperities resulting in scuffing. Contrary to Blok's model, Dyson's model predicts that the critical temperature occurs at the inlet of the contact area rather than the central region [9]. The theory presented by Dyson was further developed and referred to as critical temperature-pressure theory, since the critical temperature is a function of the lubricant pressure generated by the hydrodynamic action of the EHL contact. The validity of these theories has been explored experimentally by many, showing varied conclusions [9–15]. Several reviews have been published which contain more detail about the development and

validation of such earlier models [16–18], and even today theoretical explanations of scuffing initiation and propagation along with experimental validations are still being presented for increasingly complicated models [19–22].

With the rapid advancement of experimental and computational capabilities, publications in more recent decades have revealed through experimentation [10, 23] and numerical simulations [19, 24, 25] the importance of surface roughness in scuffing phenomenon. The occurrence of scuffing failure can be reduced by polishing the surfaces to reduce any high pressure or shear conditions within the contact zone that are induced by surface roughness. As discussed earlier, the other factors that affect the likelihood of scuffing include:

i) the operating conditions, such as load, rolling (entrainment) velocity, severity of sliding, and lubricant supply temperature

ii) lubricant properties such as viscosity, modeling of its non-Newtonian behavior (dependence on pressure, temperature, and shear), and various additives

iii) inlet blockage due to the accumulation of small wear or fatigue debris which leads to starved lubrication [14, 26]

The normal contact force between the rolling mechanical components is directly related to the contact pressure and shear applied to them. Some works [10, 19] have investigated the limiting-load for scuffing to occur (also called the scuffing load) by experimentally increasing the load applied in a step-wise manner while leaving the other contact parameters unchanged. Even under very high contact pressure, [10] showed that a scuffing failure can be avoided if operated under a low sliding condition. This is because sliding dictates not only the frictional heat which the contact surfaces will experience, but also the shear thinning behavior of the lubricant. Further, this explains why the failure location of gear teeth is consistently close to the tip or the start of the active profile (shown in Fig. 1.1)

where sliding is high while the contact force may not be maximal.

Focusing on the effects of the lubricant properties on scuffing, Jackson et al. used a disk contact machine to show that the scuffing load can be increased by using a low viscosity lubricant [15]. Further, the experimental investigation by Ichimaru et al. demonstrated that introducing certain additive combinations into the lubricant leads to the formation of protective anti-scuffing tribo-films along the contact surfaces [27]. To get to the real source of scuffing failure, Enthoven and Spikes used radiometry to visualize the onset of scuffing failure of a contact between a steel ball and a sapphire disk [9, 14, 26]. They observed an interesting mechanism - their recordings showed an accumulation of very fine wear and fatigue debris in the inlet zone, blocking the entrainment of lubricant and leading to lubricant starvation. Immediately following the debris buildup in the inlet, scuffing failure took place and the scuffing failure temperature was measured using an infrared microscope that continuously monitored the temperature distribution along the surface of the ball to be above 400°C [26].

There has been an extensive amount of research targeting the modeling and prediction of flash temperature have been conducted under the fully-flooded lubrication condition. A group of studies examined the thermal EHL behavior for perfectly smooth surfaces, specifically point contacts [28] and line contacts [29–31]. However, in each of these studies the predicted temperature increases were moderate and thus unable to explain the onset of scuffing. Further studies which incorporated the surface roughness into the thermal EHL analysis were able to deterministically predict significant flash temperature increases [19, 20, 24, 25, 32–36]. In particular, Li et al. predicted the critical flash temperature for scuffing to occur on the order of 475°C, which is comparable to the in-situ temperature measurements of Enthoven and Spikes [19, 26]; the reasonable difference is likely due to material and lubricant deviations between the studies. Specifically, [19] used an espe-

cially strong steel alloy common in aerospace applications and a modern additive lubricant which both improve the resistance to scuffing. Experimentally, the optical interferometry technique has been employed to measure the temperature distributions for smooth surface contacts [37, 38] and artificial rough contacts [39].

Under starved lubrication, many early computational [40–42] and experimental [43, 44] works stayed within the isothermal domain, excluding the flash temperature description. In a later study, Yang et al. incorporated the energy equation into the governing equations and presented a starved thermal EHL model for perfectly smooth surfaces lubricated by an Eyring non-Newtonian fluid [45]. Even more recently, Pu et al. extended the modeling effort to include the roughness effects on the flash temperature prediction for a point contact operating under starved EHL; however, this study assumed Newtonian behavior in the Reynolds equation which is not appropriate for gear contacts experiencing high sliding [46]. Further, [46] utilized the Barus equation the model the lubricant viscosity - considering that gears which are particularly vulnerable to scuffing failure are those under a heavy load, such an approximation of the viscosity dependence on pressure can substantially overestimate the viscosity and thus the viscous frictional heat. Hence, although the scuffing failure of rough surfaces under the starved lubrication condition is of great practical interest (for example, starvation caused by debris buildup [26] or by the loss of lubricant [47]), little modeling work encompassing the most realistic models for all aspects of the problem has been done.

1.3 Scope and Objectives

In view of the existing literature, a thermal EHL model with starved lubrication conditions which is capable of an accurate description of the tribological behavior under typical operating conditions for real gear surface profiles is missing. Although extensive work has

been done numerically and computationally on starved lubrication, every other work has excluded one of more practical aspect of real-world tribological conditions. Therefore, this study aims to develop an extensive thermal EHL model with starved lubrication under high sliding and high loading operating conditions for gear contacts with various engineering surface roughness profiles resultant from industrial solutions. The main objectives of this study can be summarized as:

1. Develop a numerical model based on the generalized Newtonian Reynolds equation in the thermal EHL description, incorporating measured lubricant viscosity dependencies on pressure, temperature and shear. To account for starvation, implement the cavitation algorithm proposed by Elrod in [48] to determine the starvation boundary condition.

2. Conduct simulations covering an extensive parameter space which would allow for determination of the effects of surface roughness, severity of lubrication starvation, and operating conditions on the resultant flash temperature, pressure, film thickness, friction coefficient, and power loss, as well as the instantaneous distributions of these.

3. From these relationships, demonstrate the importance of understanding tribological behavior of realistic gear profiles under different lubrication regimes and operating conditions in the context of scuffing failure.

1.4 Thesis Outline

Following this introduction, Chapter 2 explains the formulation of the computational model implemented. It covers the governing equations, relevant models, and necessary assumptions for the fluid and thermal aspects in detail. The design of the numerical simulations conducted is also discussed at length, and a table of the covered parameter space is provided. After the theoretical foundation, chapter 3 presents and discusses the results of

the simulations. It is broken into subsections which correspond to results for each major physical quantity used to characterize the tribological behavior, including temperature, film thickness, pressure, friction coefficient, power loss, and instantaneous distributions of these. Finally, chapter 4 summarizes the original research presented here, asserts concluding remarks, and proposes a direction for future work.

Model Formulation

2.1 Line Contact Equations

Consider two spur gears with base circles of radii R_1 and R_2, and applied load W as shown in Figures 1.1, 1.2, and 1.3. There are many well-known properties about the size of and pressure within the contact zone, given by:

reduced curvature: $$R' = \frac{R_1 R_2}{R_1 + R_2}$$

reduced elastic modulus: $$E' = \frac{2}{\frac{1-\nu_1^2}{E_1} + \frac{1-\nu_2^2}{E_2}}$$

pressure: $$p(x) = p^{max}\sqrt{1 - \left(\frac{x}{a}\right)^2}$$

maximum pressure: $$p^{max} = \frac{2W}{\pi a L}$$

contact zone size: $$a = \sqrt{\frac{8WR'}{\pi E' L}}$$

With these, it is also possible to derive formulas for the rigid body approach of the contacts as well as all principal and shear stresses experienced by the contacts as:

rigid body approach:
$$h_0 = \frac{2W}{\pi L E'} \left(1 + \ln\left(\frac{2\pi E' L^3}{W R'}\right)\right)$$

maximum principal stresses:
$$\sigma_x = -p^{max}\left[\left(2 - \frac{1}{\left(\frac{z}{a}\right)^2 + 1}\right)\sqrt{\left(\frac{z}{a}\right)^2 + 1} - \frac{2z}{a}\right]$$

$$\sigma_y = -2\nu p^{max}\left[\sqrt{\left(\frac{z}{a}\right)} - \frac{z}{a}\right]$$

$$\sigma_z = -p^{max}\left[\frac{1}{\sqrt{\left(\frac{z}{a}\right)^2 + 1}}\right]$$

shear stress:
$$\tau_{zx}(z) = \left|\frac{\sigma_x - \sigma_z}{2}\right|$$

maximum shear stress:
$$\tau_{max} \approx 0.3 p^{max} \quad \text{for } \nu = 0.3$$

where ν_1, ν_2 are the Poisson's ratio and E_1, E_2 are the respective elastic modulii of the gears. For more information about the derivation of these properties, refer to [2, 49]. Now, with expressions for the physical parameters of the contact zone known, focus will shift onto the fluid model for the lubricant.

2.2 Derivation of Reynolds' equation from Navier-Stokes

First derived in 1886, the Reynolds' equation is the differential equation governing the pressure distribution in the fluid film lubrication. It can be derived as a special case of the the Navier-Stokes equations for momentum conservation. The derivation will begin following a traditional control volume analysis [50], the x-component of the Navier-Stokes

equations for a Newtonian fluid is given by:

$$\rho\frac{Du}{Dt} = \rho X_a - \frac{\partial p}{\partial x} - \frac{2}{3}\frac{\partial}{\partial x}(\eta\nabla\cdot u) + 2\frac{\partial}{\partial x}\left(\eta\frac{\partial u}{\partial x}\right) + \frac{\partial}{\partial y}\left[\eta\left(\frac{\partial u}{\partial y} + \frac{\partial v}{\partial x}\right)\right] + \\ + \frac{\partial}{\partial z}\left[\eta\left(\frac{\partial u}{\partial z} + \frac{\partial w}{\partial x}\right)\right] \quad (2.1)$$

The governing equation given by (2.1) is valid for a viscous compressible flow with varying viscosity. For many problems, an analytical solution is not possible and so it is necessary to make assumptions such that (2.1) can be solved for fluid film lubrication. In general, fluid film lubrication problems are a subset of slow motion viscous flow conditions and so, through order-of-magnitude analysis of the non-dimensional form of the (2.1), it can be shown that the pressure and viscous terms dominate [50]. To derive the Reynolds' equation, need to make some key assumptions as:

1. constant viscosity, Newtonian lubricant
2. thin film geometry
3. body forces are negligible
4. no-slip boundary conditions

Let l_0, b_0, and h_0 be the characteristic lengths in the x, y, and z directions respectively. Then, can use these along with other characteristic quantities to develop a non-dimensional form of the (2.1). In this form, following an analysis comparing the magnitude of inertial and viscous forces, all terms of $\mathcal{O}(\frac{h_0}{l_0})$ and $\mathcal{O}(\frac{h_0}{b_0})$ and higher order are neglected. This leaves only the $\mathcal{O}(1)$ terms, reducing (2.1) to:

$$\frac{\partial p}{\partial x} = \frac{\partial}{\partial z}\left(\eta\frac{\partial u}{\partial z}\right) \implies u = \frac{z^2}{2\eta}\frac{\partial p}{\partial x} + A\frac{z}{\eta} + B$$

$$\text{no-slip B.C.s:} \quad u|_{z=0} = u_1 \text{ and } u|_{z=h} = u_2$$

$$\implies u = \frac{z^2}{2\eta}\frac{\partial p}{\partial x} + \frac{z}{h}\left(u_2 - u_1 - \frac{h^2}{2\eta}\frac{\partial p}{\partial x}\right) + u_1$$

Now, need to consider the continuity for unsteady flow in the x-direction for the mass content per unit film area, $\rho h\theta$, given by:

$$\frac{\partial(\rho h\theta)}{\partial t} + \frac{\partial}{\partial x}(\rho h\theta u) = 0 \tag{2.2}$$

It is more useful to consider the integral form as:

$$\int_0^h \left[\frac{\partial(\rho h\theta)}{\partial t} + \frac{\partial}{\partial x}(\rho h\theta u)\right] dz = 0$$

Integrating gives the generalized Newtonian Reynolds equation as:

$$\boxed{\frac{\partial}{\partial x}\left(\frac{\rho h^3}{12\eta}\frac{\partial p}{\partial x}\right) = u_r\frac{\partial(\rho h\theta)}{\partial x} + \frac{\partial(\rho h\theta)}{\partial t}}$$

A more generalized form which includes a fluid flow coefficient will be used in the following sections in order to incorporate the lubricant's non-Newtonian nature.

2.3 Fluid Film Flow Model

The contact of spur gears that have a small crown along the face width direction can be modeled as a line contact. Following [51–54], the unsteady one-dimensional flow of the lubricant film in the x direction between the mating surfaces is governed by the generalized Newtonian Reynolds equation as:

$$\frac{\partial}{\partial x}\left(\phi\frac{\partial p}{\partial x}\right) = u_r\frac{\partial(\rho h\theta)}{\partial x} + \frac{\partial(\rho h\theta)}{\partial t} \tag{2.3}$$

where ϕ is the flow coefficient, θ is the film fraction parameter, p is pressure, h is the film thickness, ρ is the fluid density, and t is time. The rolling velocity in the x direction is defined as $u_r = \frac{u_1+u_2}{2}$ where u_1 and u_2 are the tangential velocities of surfaces 1 and 2. Since transient effects are introduced by the time-varying surface roughness topography within the contact zone, the time related squeeze term is kept in (2.3) and t denotes time. The lubricant density ρ is pressure and temperature dependent according to [19, 20]. According

to [55], the compressibility of the lubricant can be approximated as:

$$\rho = \rho_0 \left(\frac{1 + \lambda_1 p}{1 + \lambda_2 p} \right) (1 - \lambda_3 \triangle T_f) \tag{2.4}$$

where $\lambda_1 = 2.266$ GPa^{-1}, $\lambda_2 = 1.683$ GPa^{-1}, λ_3 is the thermal expansion coefficient associated with the fluid temperature rise from the ambient temperature, which is denoted $\triangle T_f$, and ρ_0 is the fluid density under ambient pressure and temperature.

To implement the starvation/cavitation description, the fluid film fraction parameter θ proposed in [48] is implemented; this parameter represents the ratio of local fluid film density to the density under hydrodynamic pressure. To better understand how this parameter can be used in (2.3) which encompasses both the fully-flooded and starved lubrication regions, let ρh be the mass content per unit lubricant film area for a complete lubricant film at hydrodynamic pressure. Within the zone that experiences cavitation, or starved lubrication, the fluid has density ρ_c everywhere but the actual mass content is $\rho_c h \theta$ per unit area. Within the fully-flooded areas with a complete fluid film, the density varies due to fluctuations in the pressure. Hence, by slight compression, the fluid film mass content exceeds the content that would exist under hydrodynamic pressure and so $\theta = \frac{\rho}{\rho_c}$ can be used to represent this mass content fluctuation due to changes in the pressure. When the pressure drops below ambient pressure, θ becomes the unknown to be solved for following with the implementations in [41, 42, 45, 46]. With this definition, it is possible to describe starvation/cavitation without a specifying the geometry of the lubricant in the inlet of the contact zone.

For gear contacts, scuffing failure commonly takes place in the vicinity of the tooth tip where the sliding is high. Under such circumstances, the reduction of the film thickness due to the shear thinning effect is expected. Therefore, a Newtonian description of the lubricant is not sufficient. Rather, as shown in [52–54], the non-Newtonian behavior of the

lubricant can be incorporated into (2.3) through the flow coefficient ϕ as:

$$\phi = \frac{\rho h^3}{12\eta} \int_{-1/2}^{1/2} \hat{z}\hat{\tau} f(\hat{\tau}) d\hat{z} \tag{2.5}$$

$$= \frac{\rho h^3}{12\eta} \int_{-1/2}^{1/2} \frac{\hat{z}\tau}{G} \left(1 + |\hat{\tau}|^{\beta}\right)^{\frac{1-n}{\beta n}} d\hat{z} \tag{2.6}$$

where $\hat{z}$ is the dimensionless coordinate defined by $\hat{z} = \frac{z}{h}$ with z pointing from surface 1 to surface 2 across the film thickness direction. The origin of the z axis is set at the midpoint along the film thickness such that $z = -\frac{h}{2}, \hat{z} = -\frac{1}{2}$ at surface 1 and $z = \frac{h}{2}, \hat{z} = \frac{1}{2}$ at surface 2; the x axis goes along the length of the contact zone. The function $f(\hat{\tau})$ is referred to in the literature as the shear-thinning function, and uses a modified Carreau model for the non-Newtonian behavior of the lubricant. In (2.6), the lubricant low-shear viscosity, denoted η, is dependent on the pressure and the temperature T_f and can be modeled according to [56] as:

$$\eta = \eta_{0\infty} \left(1 + \frac{\hat{\alpha}_0 p}{q}\right) \exp\left(\frac{C_F p}{p_\infty - p}\right) \exp\left(\frac{D_F T_{f\infty}}{T_f - T_{f\infty}}\right) \tag{2.7}$$

where

$$\hat{\alpha}_0 = a_0 - \frac{a_1}{T_f} + \frac{a_2}{T_f^2}$$
$$q = b_0 + \frac{b_1}{T_f}$$
$$p_\infty = c_0 + \frac{c_1}{T_f}$$

To fully define and understand (2.6), also need the Newtonian limit shear stress G, the shear rate sensitivity coefficient n, and the Yasuda parameter β. All of these constants involved in (2.6) and the others involved in (2.7) are lubricant dependent parameters. For specific values, refer to Table 8.1 in [57].

2.4 Numerical Unification

For gear contacts, asperity interaction occurs frequently because of significant surface roughness that results from machining of the gears. In the local asperity contact regions, the Reynolds equation fails as the assumption of a continuum fluid is no longer valid. Within these areas of asperity interaction, the hydrodynamic lubrication film is replaced by a boundary lubrication one which is assumed to have constant thickness such that:

$$\frac{\partial h}{\partial x} = 0 \tag{2.8}$$

With the gradient of the film thickness along the x direction zero, it is possible to establish a unified numerical system to solve the nonlinear governing equations robustly and accurately as shown in [25, 46, 58–61]. The film thickness h in (2.3) and (2.8) is governed by the rigid body approach of the two solid surfaces h_0, the separation between the surfaces before any elastic deformation takes place g_0, the elastic deformation V, and the surface roughness heights of surfaces 1 and 2, s_1 and s_2 respectively, as:

$$h = h_0 + g_0 + V - s_1 - s_2 \tag{2.9}$$

as shown in [58, 59, 61]. The total elastic deformation $V(x,t)$ induced by $p(x,t)$ is given by:

$$V(x,t) = \int_{x_s}^{x_e} K(x - x')p(x',t)dx' \tag{2.10}$$

where x_s and x_e are the start and end points of the computational domain of the contact zone, and $K(x) = -\frac{4\ln|x|}{\pi E'}$ is the influence function [62]. This is called Boussinesq's half space formulation and assumes that the contact zone is relatively small and the surfaces are smooth. Further, for the line contact under consideration the separation g_0 is given by:

$$g_0 = \frac{x^2}{2R'}$$

The rigid body approach is determined by applying the equilibrium condition along the normal force direction, equating the total contacting force due to the distributed pressure over the entire contact zone to the applied normal load. Thus, the load balance equation is given by

$$W = \int_{\Gamma} p(x,t)dx \tag{2.11}$$

where Γ is the computational domain.The expression in (2.11) is used as a check for the load balance convergence of the solution. The rigid body approach h_0 in (2.9) is adjusted within a load iteration loop until (2.11) is satisfied.

2.5 Heat Transfer Model

Considering that the lubricant density and viscosity is temperature dependent, as shown by (2.4) and (2.7), the temperature distribution of the fluid within the contact zone is of interest. To find this distribution, a simplified form of the fluid energy equation which neglects heat convection across the fluid film. heat conduction along the rolling direction, and compressive temperature fluctuations is used as:

$$k_f \frac{\partial^2 T_f}{\partial z^2} + \tau\dot{\gamma} = \rho c_f \left(u\frac{\partial T_f}{\partial x} + \frac{\partial T_f}{\partial t} \right) \tag{2.12}$$

where k_f and c_f are the lubricant thermal conductivity and specific heat respectively, and the shear strain rate $\dot{\gamma}$ is given by:

$$\dot{\gamma} = \left(\frac{\tau}{\eta}\right) f(\hat{\tau}) = \left(\frac{\tau}{\eta}\right) \left(1 + |\hat{\tau}|^{\beta}\right)^{\frac{1-n}{\beta n}}$$

Since scuffing failure of gears is associated with high surface velocities, the shear flow dominates and thus the variation of the fluid velocity along the film thickness direction can

be approximated linearly as:

$$u = u_1(1 - \hat{z}) + u_2\hat{z}$$

In order to reduce the necessary computational efforts, the parabolic relationship for the fluid temperature distribution along the $\hat{z}$ direction proposed by Kim and Sadeghi [63] is adopted as:

$$T_f = (3T_1 + 3T_2 - 6T_m)\hat{z}^2 - (4T_1 + 2T_2 - 6T_m)\hat{z} + T_1$$

where T_m is the mean temperature of the fluid across the film thickness, $T_i, i = 1, 2$ is the temperatures of surface i and is composed of the surface bulk temperature T_i^b and flash temperature rise $\triangle T_i$ as:

$$T_1 = T_1^b + \triangle T_1$$

$$T_2 = T_2^b + \triangle T_2$$

The surface bulk temperature is assumed to be fixed as the lubricant supply temperature, while the flash temperature rise is dictated by the frictional heat flux Q_i according to [64] as:

$$\triangle T_i(x,t) = \int_t dt' \int_x \exp\left\{ -\frac{[(x - x') - u_i(t - t')]^2}{4\kappa_s(t - t')} \right\} \frac{Q_i(x', t')dx'}{2\pi k_s(t - t')} \tag{2.13}$$

where κ_s and k_s are the thermal diffusivity and conductivity of the solid surface respectively. The heat partition coefficient ϑ is used to partition the total heat flux Q into each of the bounding surfaces. It is determined according to the boundary condition

$$T_1 - T_2 = \frac{h}{2k_f}(1 - 2\vartheta)Q \tag{2.14}$$

presented by [24], and partition the heat flux such that

$$Q_1 = \vartheta Q$$

$$Q_2 = (1 - \vartheta)Q$$

Wherever the hydrodynamic fluid film breaks down (h = 0), (2.14) reduces to $T_1 = T_2$ implying a continuous temperature transition at the surface interface. Within the hydrodynamic fluid areas, the total heat flux is obtained by performing integration as

$$Q = \int_{-h/2}^{h/2} \tau \dot{\gamma} dz$$

and within areas of asperity interaction, have

$$Q = \mu_b p |u_1 - u_2|$$

where the boundary lubrication friction coefficient $\mu_b = 0.1$ in this study following [19, 32, 60, 65].

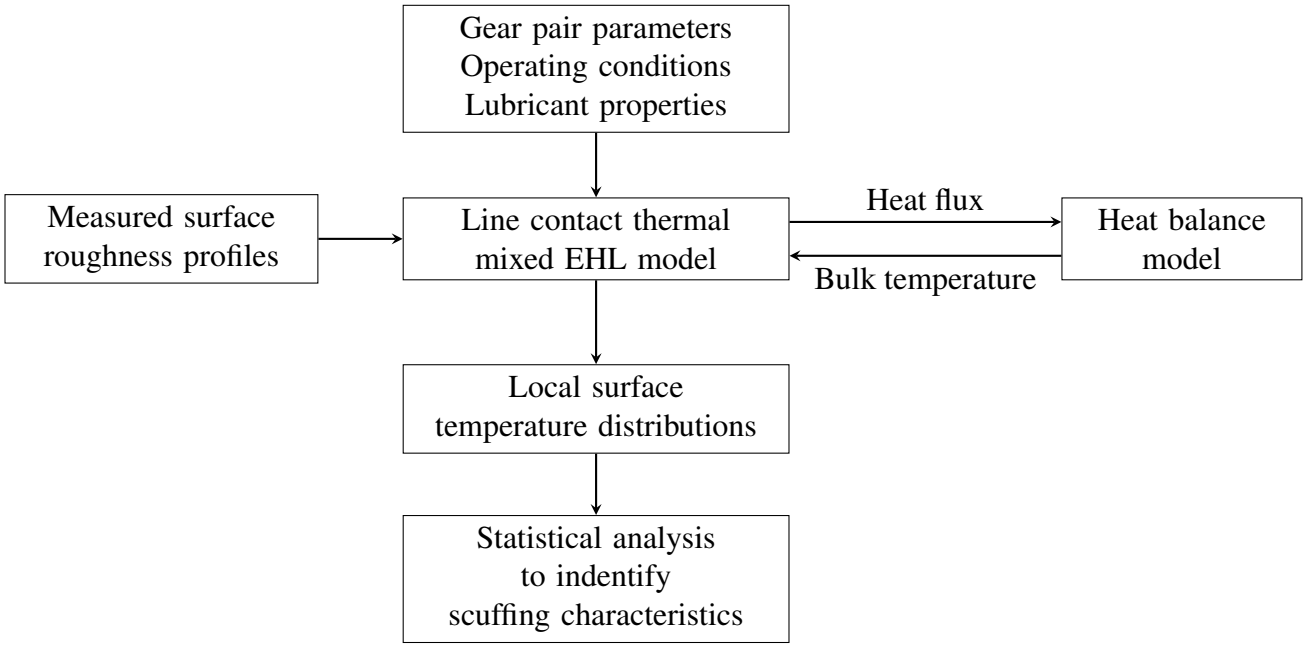

Figure 2.1: Modeling methodology for scuffing failure simulations of line contact.

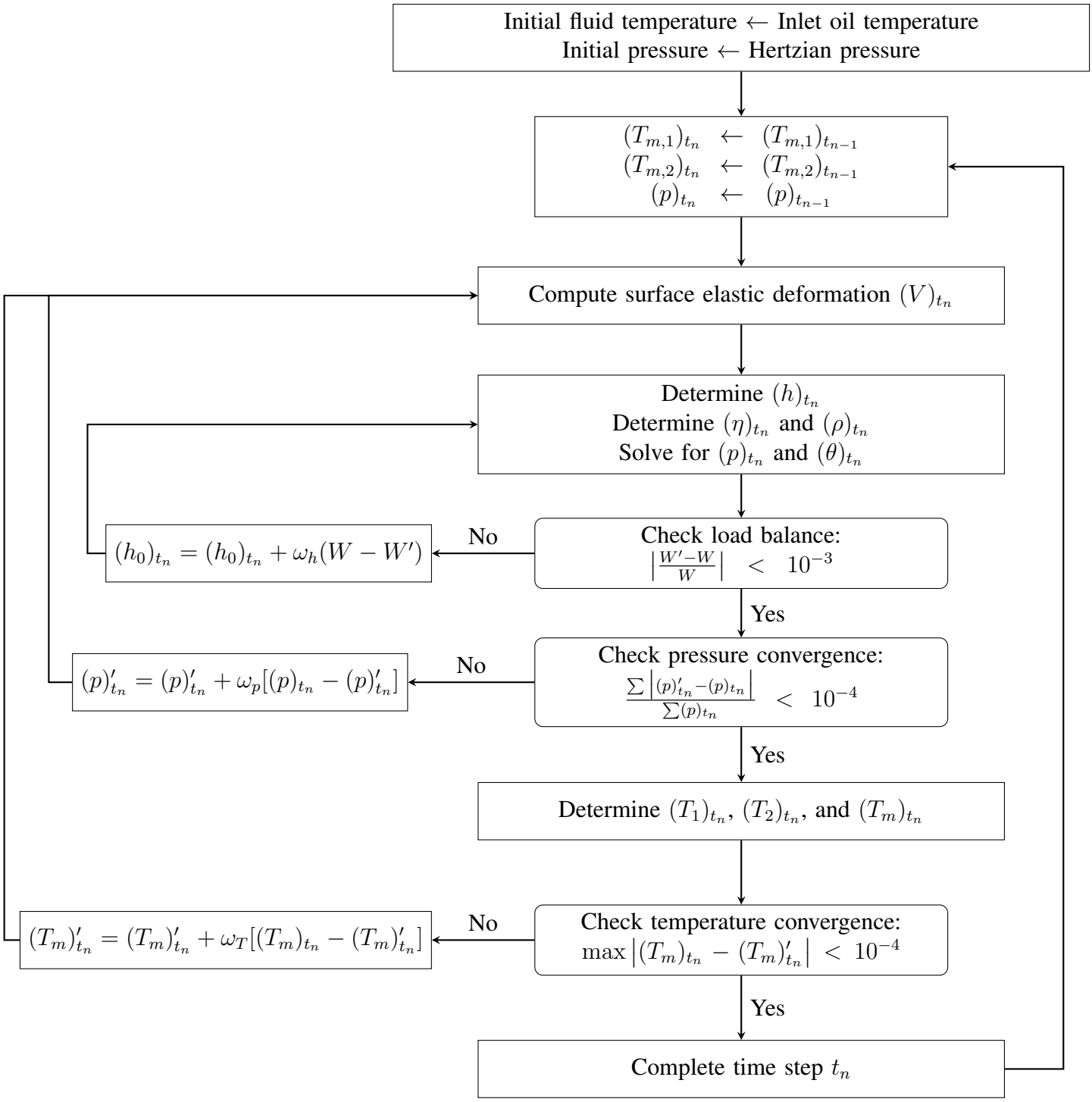

Figure 2.2: Flowchart of thermal mixed EHL computation.

2.6 Simulation Design and Discussion

This study models the lubrication behavior of a line contact characterized by a reduced radius of curvature of $r' = 7.5$ mm, under the operating conditions shown by Table 2.1. The normal force density and the inlet lubricant temperature are kept unchanged at $W = 590$ N/mm and $T_{in} = 100°$C respectively, which correspond to the Hertzian pressure of $p_h = 1.7$ GPa and the Hertzian half width $a_h = 0.22$ mm. A total of four velocity conditions are considered; two rolling velocities of $u_r = 7.5$ and 15 m/s together with two slide-to-roll ratios of $SR = -1$ and -0.5. These operating conditions were chosen because they are typical of high speed gearing applications which are potential candidates for scuffing failure.

For all simulations the computational domain is $x_s = -2.5a_h \leq x \leq 1.5a_h = x_e$ where a_h is the half the width of the Hertzian contact area. To investigate the effects of lubrication starvation on the tribological behavior with respect to the flash temperature, the fluid film fraction parameter θ^{in} takes on ten values as $\theta^{in} = 1$, 0.5, 0.15, 0.09, 0.05, 0.03, 0.02, 0.015, 0.01, and 0.005, where $\theta^{in} = 1$ represents the full flooded lubrication condition (i.e. no starvation) and $\theta^{in} = 0.05$ represents an extremely starved lubrication condition. To better understand the physical meaning of the fluid film fraction parameter, Figure 2.3 shows the shape of the lubrication film between the contact surfaces, where the film of lubricant attached to each surface at the beginning of the computational domain has thickness h_1^{in} and h_2^{in} for surfaces 1 and 2 respectively. Air takes up the space between these two fluid layers in the inlet and outlet zones. With the gap between the solid surfaces at the beginning of the computational domain defined as g^{in} as shown in Figure 2.3, the fluid film fraction parameter is defined as

$$\theta^{in} = \frac{h^{in}}{g^{in}} \tag{2.15}$$

where

$$h^{in} = h_1^{in} + h_2^{in}$$
$$g^{in} = h_0 + \frac{x_s^2}{2r'}$$

From this, the rigid body approach h_0 is numerically determined following [58–61]. Corresponding to the extremes of the selected θ^{in} range, the inlet fluid film thickness varies as $0.07\mu\text{m} \leq h^{in} \leq 14.03\mu\text{m}$. The final parameter which varied between simulations was the surface roughness. In order to analyze the effects of increased asperity presence, four surface roughness profiles were used: a ground surface, a polished surface, a highly polished surface, and an idealized, smooth surface. The profiles of the three surfaces with differing asperity magnitudes are shown in Figure 2.4. The operating conditions described and shown in Table 2.1 yield a total of forty combinations, which were repeated for the four surface roughness conditions yielding one hundred and sixty total simulations. The

velocity values and terminology used to refer to different operating conditions are shown in Table 2.2.

The roughness profiles shown in Figure 2.4 were measured from cylindrical roller specimens along the circumferential direction using a Form Talysurf surface profiler. The root mean square roughness amplitudes are $R_q = 0.3, 0.11, 0.06\ \mu$m for the ground, polished, and highly polished surfaces respectively. This study also utilizes a typical turbine fluid, MIL-L23699, whose viscosity dependencies on pressure, temperature, and shear stress were fully characterized by experimental measurements [52, 53].

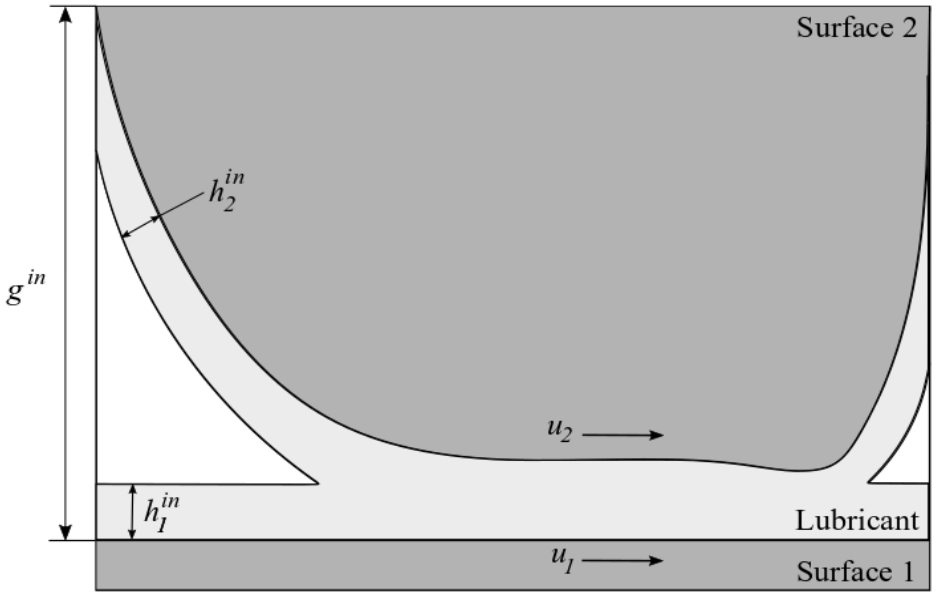

Figure 2.3: Schematic view of thin lubrication film for EHL contacts.

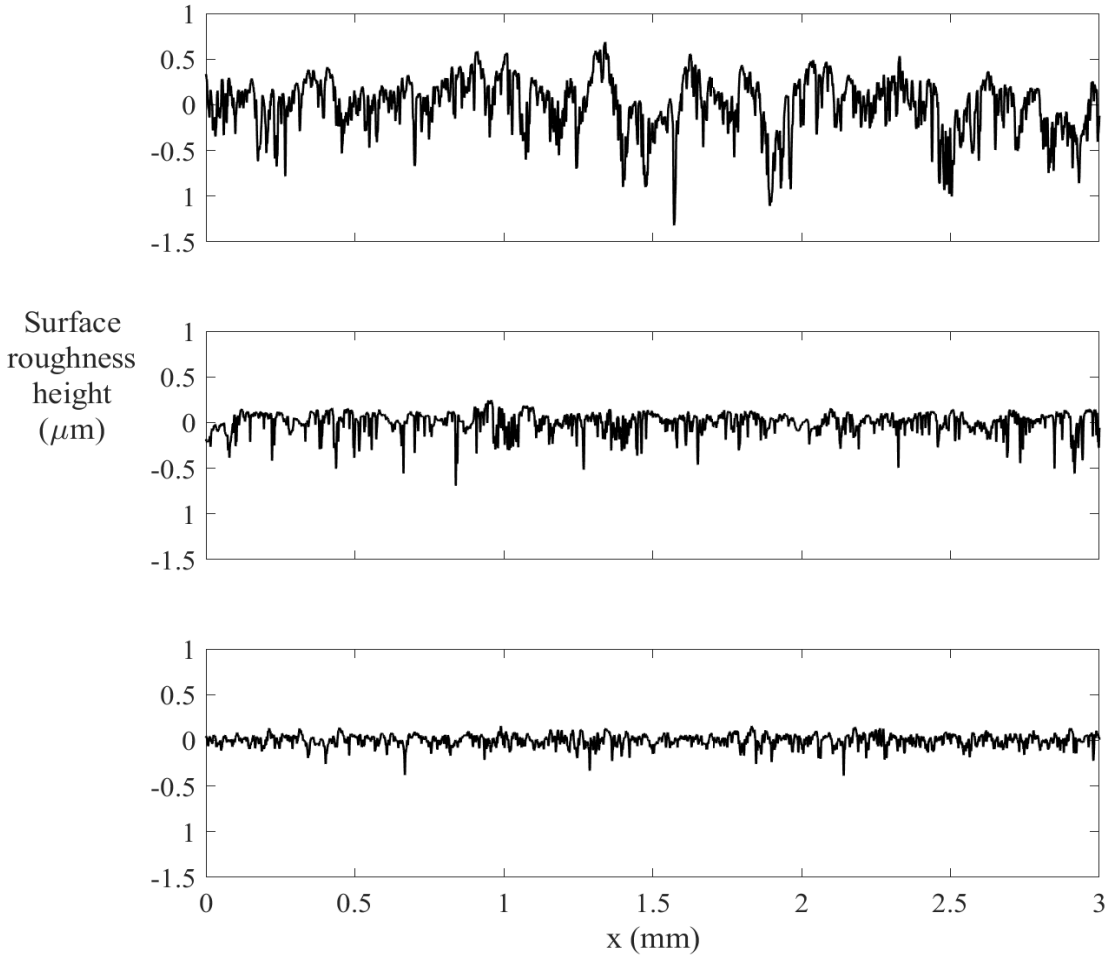

Figure 2.4: Surface roughness profiles of ground, (top, $R_q = 0.3\mu$m), polished, (middle, $R_q = 0.11\mu$m), and highly polished (bottom, $R_q = 0.06\mu$m) surfaces.

Force density, $W[\frac{N}{mm}]$	590
Hertzian pressure, $p_h[GPa]$	1.7
Hertzian half width, $a_h[mm]$	0.22
Inlet lubricant temperature, $T_{in}[^\circ C]$	100
Rolling velocity, $u_r[\frac{m}{s}]$	7.5, 15
Slide-to-roll ratio, SR	-1, -0.5
Film fraction boundary condition, θ^{in}	1, 0.5, 0.15, 0.09, 0.05, 0.03, 0.02, 0.015, 0.01, 0.005
Surface roughness	ground, polished, highly polished, and smooth

Table 2.1: Simulation matrix.

terminology	u_r (m/s)	SR	u_1 (m/s)	u_2 (m/s)
high speed, high sliding	15	-1	7.5	22.5
high speed, low sliding	15	-0.5	11.25	18.75
low speed, high sliding	7.5	-1	3.75	11.25
low speed, low sliding	7.5	-0.5	5.625	9.375

Table 2.2: Velocity values and terminology corresponding to different operating conditions.

Simulation Results and Discussion

Due to the evolution of the surface roughness profiles, the tribological behavior within the contact zone is transient and hence so are the physical quantities which characterize it such as the distributions of the temperature, pressure, film thickness, friction coefficient, and power loss. Methods of data analysis for each quantity and discussion of their physical implications follow in the next sections.

3.1 Effects of Starvation on Temperature

In order to study how temperature changed with asperity interaction resultant from the different surface roughness profiles, the maximum temperature of surface 1, ${T_1}^{max}$, is shown as a function of the asperity contact force ratio χ_W in Figure 3.1. The asperity contact ratio is defined as the ratio of the force supported by the asperity contacts to the total normal force. In particular, Figure 3.1 shows results corresponding to the ground surface finish under the operating conditions $u_r = 15$ m/s and $SR = -1$. Remark that these are the operating conditions which induce the most sliding between the surfaces and will be used repeatedly to show the extremes of the tribological behavior. As covered in the literature review, experimental results show that surface flash temperatures above $400°C$ can be used a criteria to establish the onset of scuffing failure. This is the motivation behind the red dashed lines on Figures 3.1, 3.2, and 3.3 indicating $400°C$. In 3.1, there are multiple instances where the maximum surface temperature rises above the scuffing criteria - in fact, it happens for every operating condition where $\theta^{in} \leq 0.05$. For comparison, Figures 3.2 and 3.3 show the same quantities for the polished and highly polished surfaces respectively under the same operating conditions. Observe that the temperatures in Figure 3.1 are relatively high compared to Figures 3.2 and 3.3, and neither of the latter figures show any occurrence of temperatures high enough to pass the scuffing threshold. The maximum value of T_1 with respect to both temporal and spatial resolutions is shown in 3.4 - this further highlights that the maximum temperature is $\sim 440°C$ for $\theta^{in} \leq 0.05$.

With respect to the surface roughness profiles, the substantial variations of ${T_1}^{max}$ with χ_W over time shown in Figure 3.1 can be attributed to the significant surface roughness height fluctuations of the ground surface. The other trend of interest in both Figures 3.1

and 3.3 is the change in ${T_1}^{max}$ as the severity of lubrication starvation is increased. The most starved case where $\theta^{in} = 0.05$ shows a substantial increase in the maximum surface temperature as compared to the fully flooded case, i.e. $\theta^{in} = 1$. Both figures show a dramatic increase in the asperity contact activity as θ^{in} is decreased, contributing to the increase of ${T_1}^{max}$. Another way to examine the flash temperature variation is through the statistical analysis proposed by Li et al. which constructs the probability density distribution of ${T_1}^{max}$ to better visualize the variations with starvation severity [19].

Figures 3.5, 3.6, and 3.7 show the probability density distributions of ${T_1}^{max}$ for all starvation conditions, operating at $u_r = 15$ m/s and $SR = -1$, for the ground, polished, and highly polished surfaces respectively. Each of these show that ${T_1}^{max}$ approximately follows a Gaussian or normal distribution; this was supported by a lack of rejection by Kolmogorov-Smirnov tests with $\alpha = 0.05$ level of significance. The associated standard deviations generally increase as θ^{in} decreases and the surface roughness becomes more severe. This is a result of the increased asperity interaction as both the roughness amplitude and the starvation severity increases.

To fully characterize the flash temperature variation with the starvation severity, the median of the ${T_1}^{max}$ distribution, denoted $\bar{T}_1{}^{max}$, is shown as a function of θ^{in} in Figure 3.8 for all operating condition and surface profile combinations. It is shown that the high rolling velocity ($u_r = 15$ m/s) and high slide-to-roll ratio ($SR = -1$) yield higher flash temperatures as compared to the low rolling ($U_r = 7.5$ m/s) and low slide-to-roll ratio ($SR = -0.5$) cases. This is a direct result of the elevated shear rate in the lubricated areas and the increased sliding velocity in the asperity contact areas, which contribute to the viscous and boundary friction heat flux respectively. For the three engineering surface finishes (ground, polished, and highly-polished), the ground surface which has the highest roughness amplitude produces the highest flash temperature. When the surface is polished, reducing R_q from 0.3 μm to 0.11 μm, the flash temperature decreases substantially; the reduction is much less when the surface is highly polished to R_q of 0.06 μm. Figure 3.8 also shows that the median maximum temperature of surface 1 does not increase immediately as θ^{in} decreases; rather, a dramatic increase is shown beyond θ^{in} = 0.09, 0.05, and 0.03 for the ground, polished, and highly-polished surfaces respectively. This trend is replaced by asymptotic behavior for θ^{in} = 0.03, 0.01, and 0.005 for the ground, polished, and highly-polished surfaces respectively.

3.2 Effects of Starvation on Film Thickness

To investigate the underlying cause of the relationship between $\bar{T}_1{}^{max}$ and θ^{in} shown in Figure 3.8, the average film thickness within the nominal Hertzian zone, defined as:

$$h_{avg} = \int_{-a_h}^{a_h} \frac{h}{2a_h} dx$$

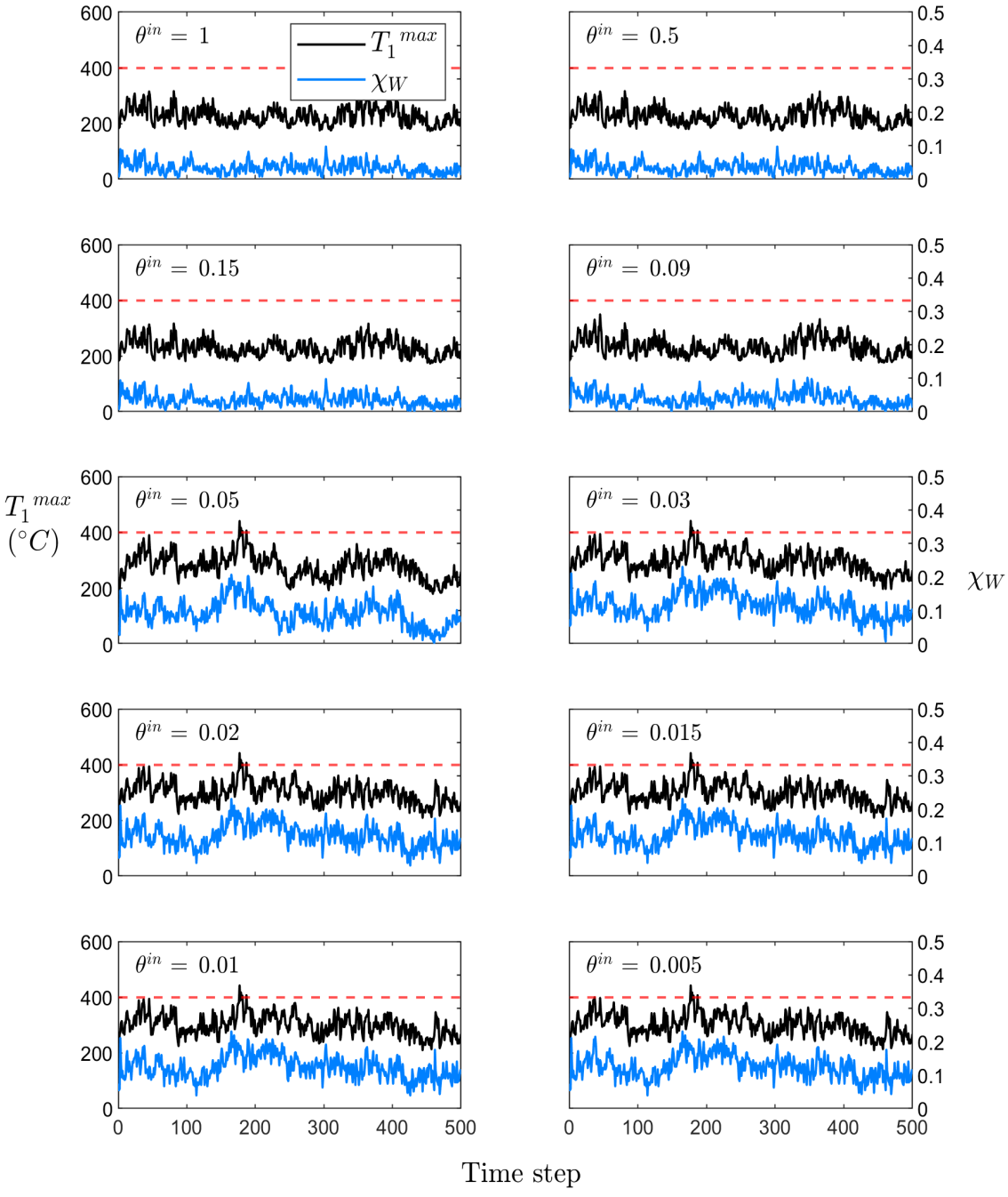

Figure 3.1: Variations of $T_1{}^{max}$ with χ_W for all film fraction boundary conditions for the ground surface under operating conditions $u_r = 15$ m/s and $SR = -1$.

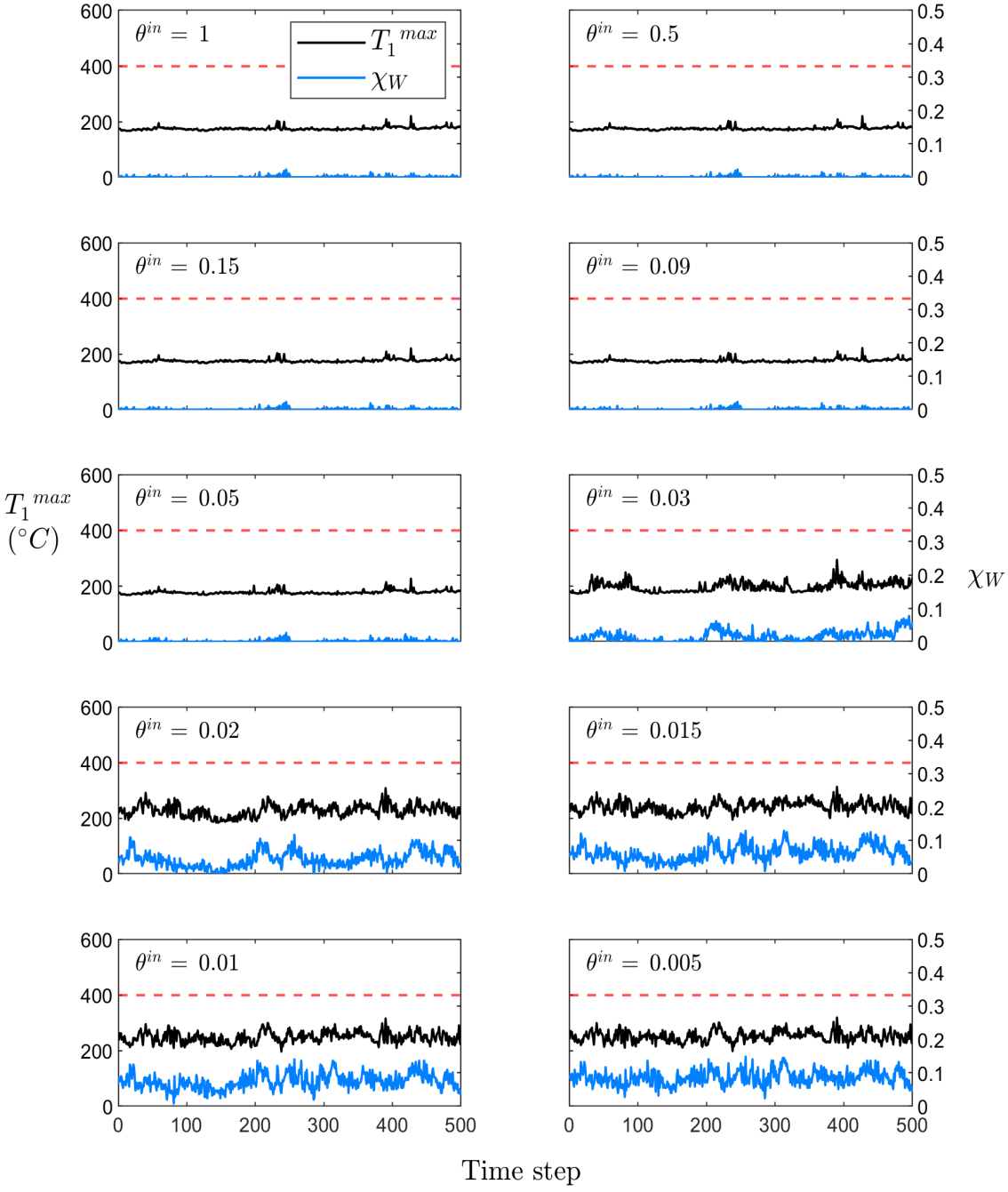

Figure 3.2: Variations of $T_1{}^{max}$ with χ_W for all film fraction boundary conditions for the polished surface under operating conditions $u_r = 15$ m/s and $SR = -1$.

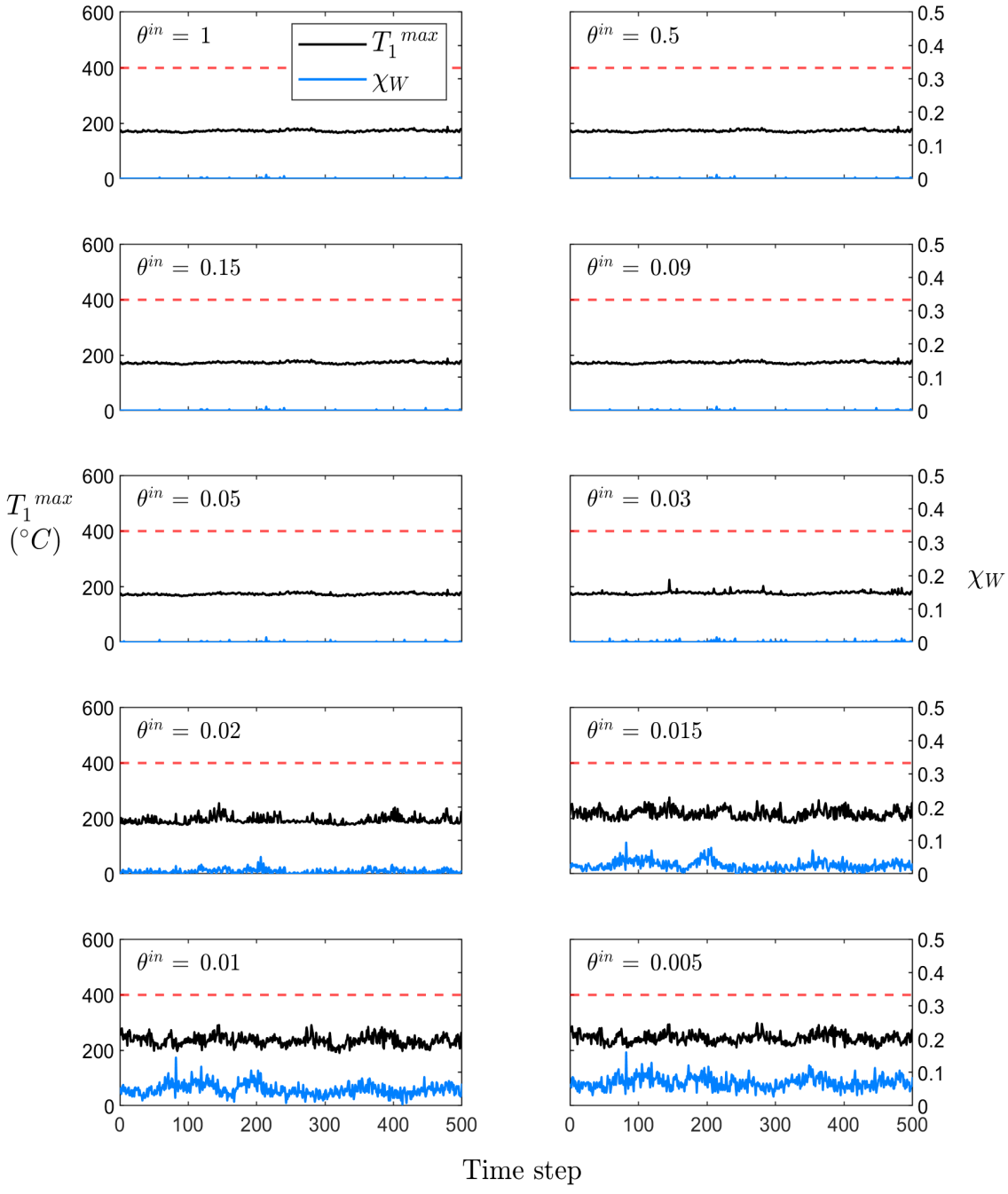

Figure 3.3: Variations of $T_1{}^{max}$ with χ_W for all film fraction boundary conditions for the highly polished surface under operating conditions $u_r = 15$ m/s and $SR = -1$.

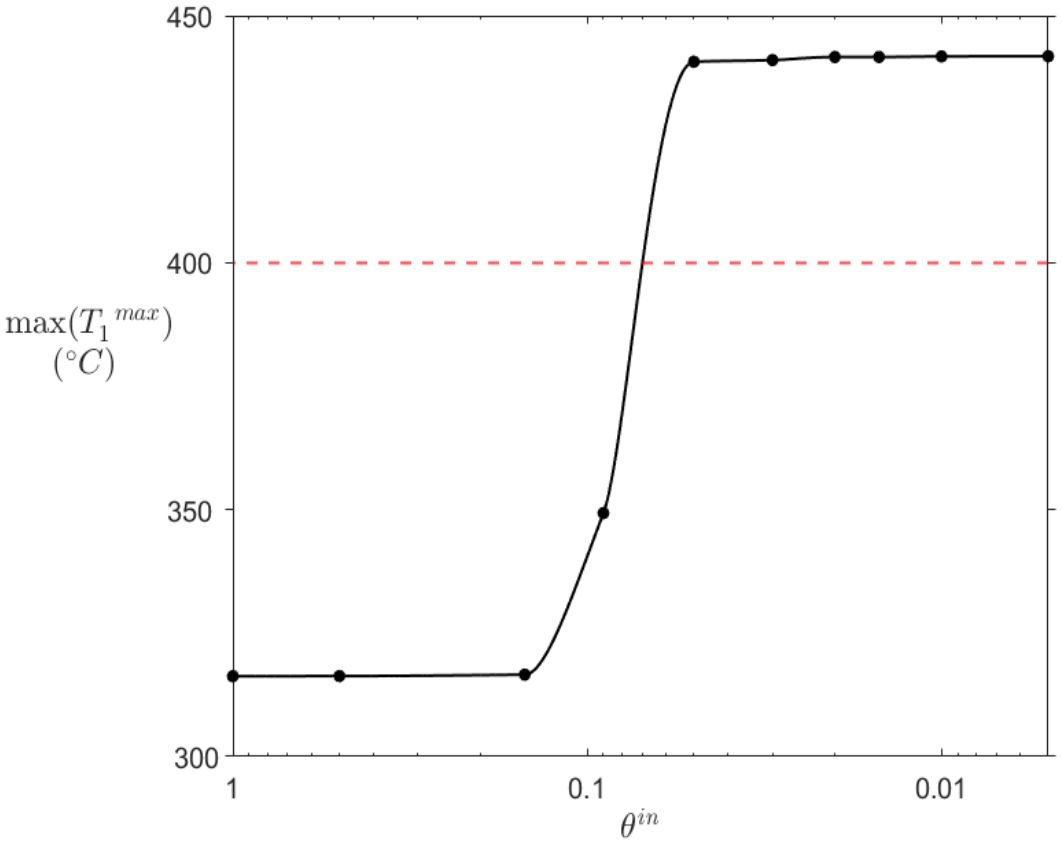

Figure 3.4: Worst-case scenario: maximum value of $T_1{}^{max}$ against $theta^{in}$ for all film fraction boundary conditions for the ground surface under operating conditions $u_r = 15$ m/s and $SR = -1$.

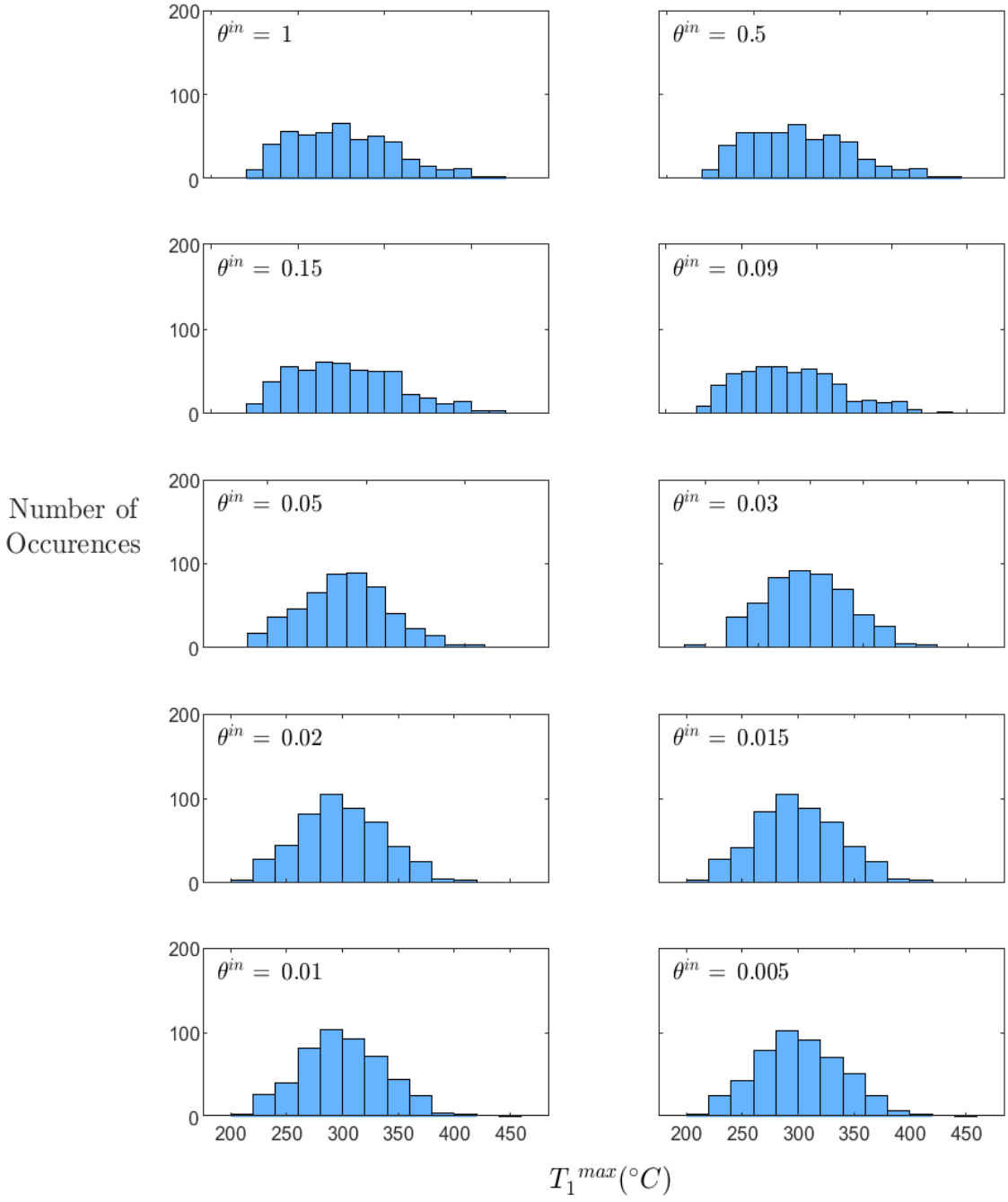

Figure 3.5: Probability density distribution of $T_1{}^{max}$ for all film fraction boundary conditions under operating conditions $u_r = 15$ m/s, $SR = -1$, and the ground surface.

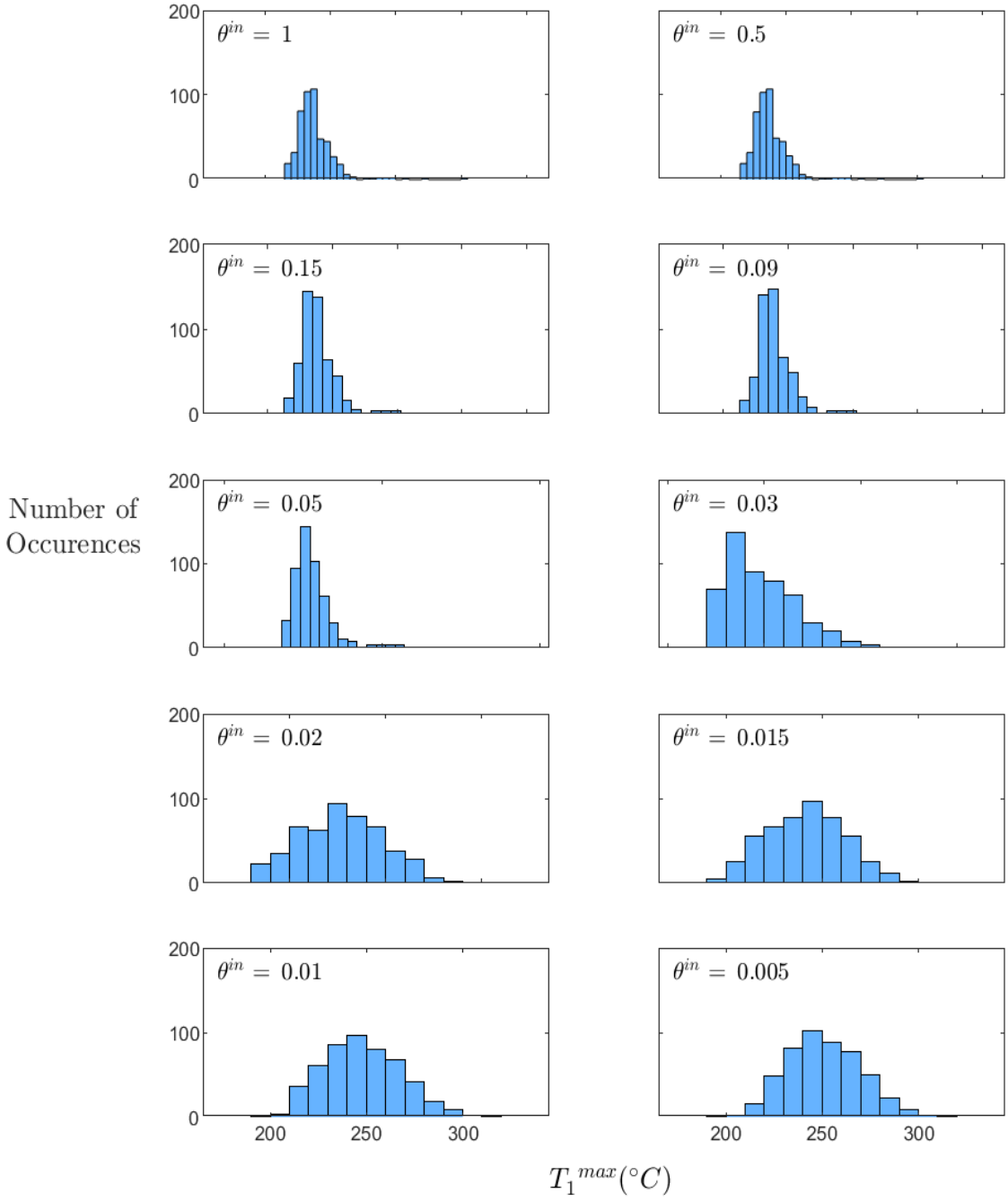

Figure 3.6: Probability density distribution of $T_1{}^{max}$ for all film fraction boundary conditions under operating conditions $u_r = 15$ m/s, $SR = -1$, and the polished surface.

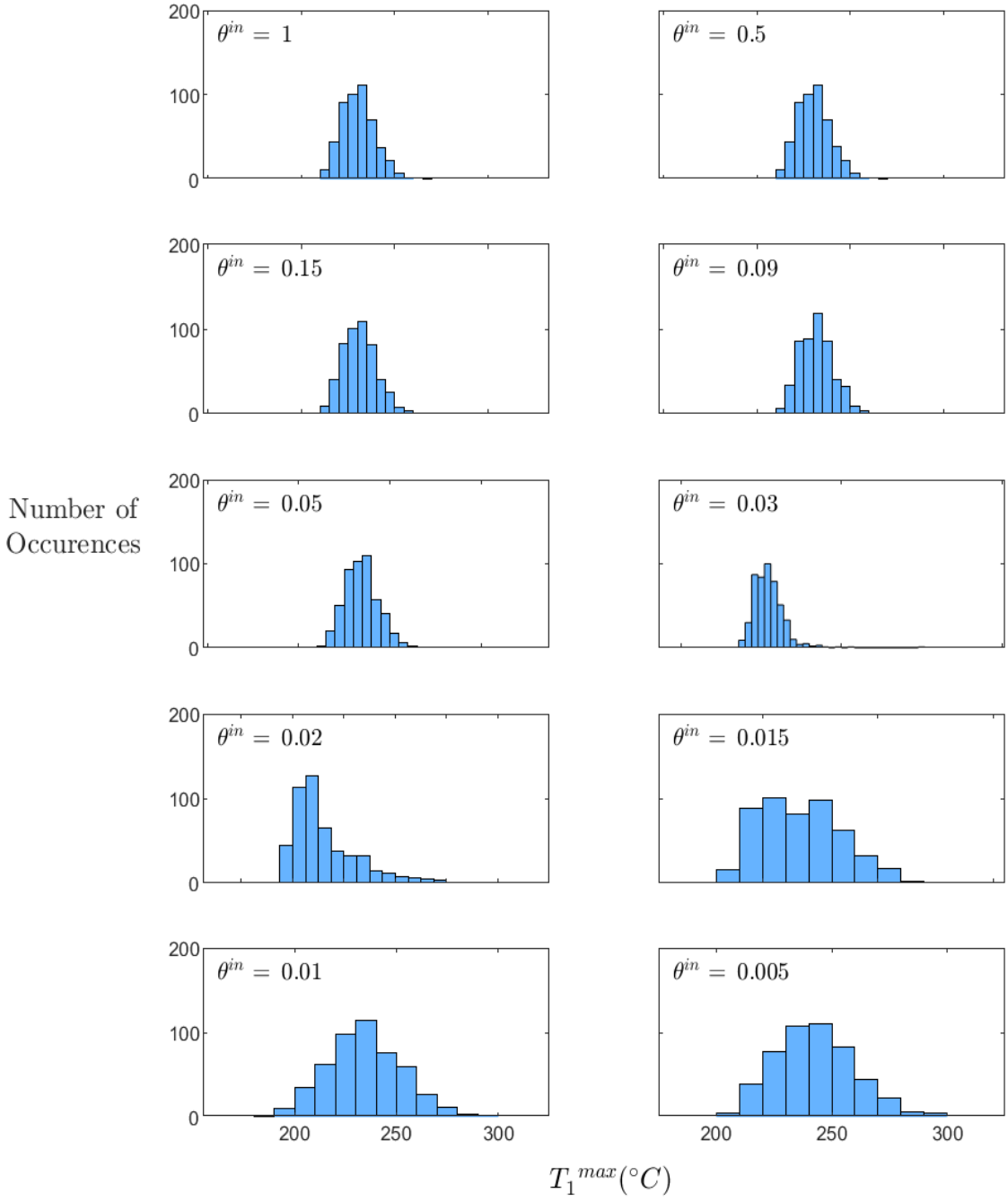

Figure 3.7: Probability density distribution of $T_1{}^{max}$ for all film fraction boundary conditions under operating conditions $u_r = 15$ m/s, $SR = -1$, and the highly polished surface.

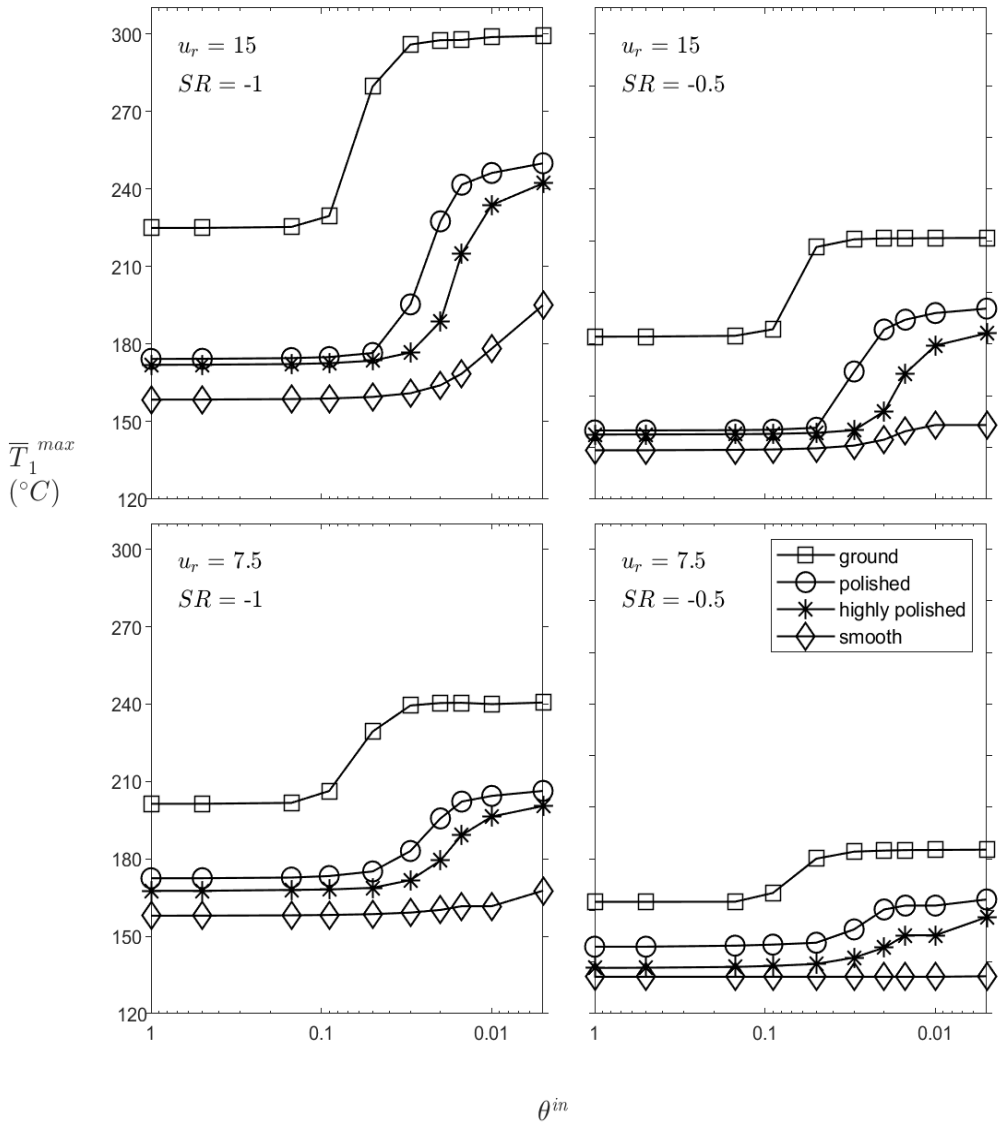

Figure 3.8: Variations of $\bar{T}_1{}^{max}$ with θ^{in} under various operating conditions.

was calculated. Then, the median of h_{avg}, denoted $\bar{h}_{avg}$, was found and plotted as a function of θ^{in} and the inlet film thickness h^{in} in Figure 3.9. This figure shows the contact for all different operating condition and surface roughness profiles. Under the fully flooded condition, i.e. $\theta^{in} = 1$, the median average film thickness, denoted $\bar{h}_{avg}^{fld}$ was found to decrease as the roughness amplitude decreased for each operating condition as shown in Table 3.1. The larger median average film thickness for the ground surface, i.e. the roughest surface, is due to the larger peak to valley height of the surface profile as shown by Figure 2.4. The larger peak to valley height keeps the two surfaces separated and prevents them from coming too close to each other, which would create excessive contact pressures thus allowing the equilibrium condition to be reached along the normal force direction.

To better understand the dependencies at play, consider the ground surface under the highest sliding operating conditions shown in the top left subplot in Figure 3.9. It is shown that when $\theta^{in} = 0.15$, the supply lubrication film thickness h^{in} = 2.1 μm which is much larger than $\bar{h}_{avg}^{fld} = 0.43\mu$m. As a result, $\bar{h}_{avg}$ remains unchanged in Figure 3.9 which explains why $T_1{}^{max}$ is not affected when θ^{in} decreases from 1 to 0.15 in Figure 3.8. Continuing to decrease θ^{in} to 0.09, 0.05, and 0.03, Figure 3.9 shows a reduction in h^{in} to 1.3, 0.7, and 0.4 μm respectively, approaching $\bar{h}_{avg}^{fld}$. Under these circumstances, the starvation impacts the lubrication film thickness resulting in a substantial drop in $\bar{h}_{avg}$ which corresponds to the large flash temperature increase in the top left subplot of Figure 3.8. However, as θ^{in} is further reduced, Figure 3.9 shows that the median average film thickness maintains its value, even as h^{in} becomes 0.07 μm at $\theta^{in} = 0.05$ which is much smaller than $\bar{h}_{avg}^{fld}$.

This second region of flatness in $\bar{h}_{avg}$ when θ^{in} is small is due to the small roughness heights of the two mating surfaces which do not permit further rigid body approach to ensure that the equilibrium condition is satisfied. The same behavior is observed for the other two engineering surfaces. The median average film thickness decreases slightly when θ^{in} decreases below 0.05, 0.03, and 0.01 for the polished, highly polished, and smooth surfaces respectively. The marked decrease of $\bar{h}_{avg}$ for the smooth surface under all operating conditions is due to the absence of surface roughness which allows for the most rigid body approach. An interesting behavior to remark is that the values of h^{in} that correspond to the second region of flatness in $\bar{h}_{avg}$ as θ^{in} becomes small are 0.4, 0.14, and 0.07 μm for the ground, polished, and highly polished surfaces respectively; these are very similar to the corresponding composite surface roughness RMS amplitudes, R_q^c for the three engineering surfaces which are $R_q^c = 0.42, 0.16$, and 0.08 μm respectively.

$\bar{h}_{avg}^{fld}$ (μm)	$u_r = 15$ m/s $SR = -1$	$u_r = 15$ m/s $SR = -0.5$	$u_r = 7.5$ m/s $SR = -1$	$u_r = 7.5$ m/s $SR = -0.5$
ground	0.43	0.42	0.39	0.38
polished	0.24	0.25	0.18	0.18
highly polished	0.22	0.22	0.15	0.15
smooth	0.20	0.21	0.13	0.13

Table 3.1: Median average film thickness under fully flooded lubrication condition, $\bar{h}_{avg}^{fld}$, for each surface roughness and operating condition.

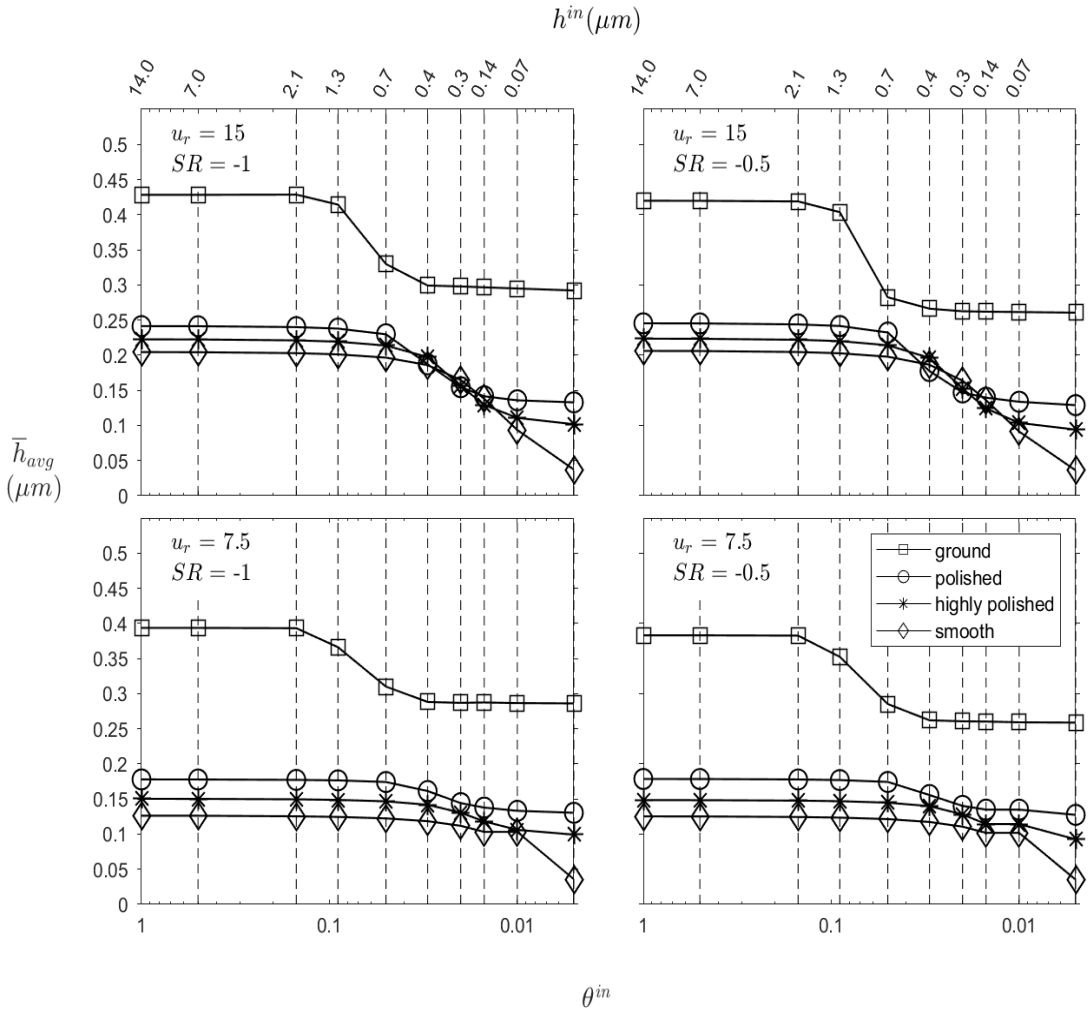

Figure 3.9: Variations of $\bar{h}_{avg}$ with θ^{in} and h^{in} under various operating conditions.

3.3 Effects of Starvation on Pressure

Considering the time varying surface roughness profiles within the contact zone, the maximum contact pressure, p^{max}, is unsteady and its probability density distribution is also Gaussian similar to that of $\bar{T_1}^{max}$. Following Figures 3.5, 3.6, and 3.7, the probability density distributions of maximum contact pressure for the ground, polished, and highly polished surface profiles under the operating conditions $u_r = 15$ m/s and $SR = -1$ are shown in Figures 3.10, 3.11, and 3.12 respectively. The median of the maximum contact pressure, $\bar{p}^{max}$, follows in Figure 3.13. It is observed that the pressure increases as the starvation severity is increased, i.e. as θ^{in} in decreased. Since the contact pressure dictates the rolling contact fatigue failure, the relationship observed between $\bar{p}^{max}$ qualitatively explains the experimentally measured asymptotic relationship between contact fatigue life and lubricant flow rate shown in [66]; in their experiments, Querlioz et al. controlled the flow rate to arrive at different starvation conditions. Figure 3.13 also shows that the pressure is significantly elevated under high sliding operating conditions since both cases with $SR = -1$ show higher magnitude pressures as compared to those where $SR = -0.5$. This shows an important shear thinning effect - as the viscosity of a shear thinning lubricant decreases, the film thickness height will decrease thus increasing the contact pressure. Comparing across the different surface roughness profiles, it is clear that the ground surface results in much larger contact pressure than the other surfaces; further, the pressure difference between the polished and highly-polished surfaces is relatively small. This is also shown by Figures 3.14, 3.15, and 3.16 which allow for comparison of changes in the behavior of p^{max} with θ^{in} for the different surface roughness profiles. In comparison to the smoother surfaces, the contact pressure in Figure 3.14 is relatively elevated and the most dependent on the asperity interaction for all values of θ^{in}. For the polished and highly-polished surfaces, the contact pressure profile remains largely unchanged for the larger values of θ^{in} and only shows slight change for $\theta^{in} < 0.05$. For all surface roughness profiles it is clear that as the starvation severity is increased the asperity interaction becomes more important and hence more closely dictates the contact pressure behavior.

3.4 Effects of Starvation on Friction Coefficient

The friction coefficient μ is the ratio of the friction force between surfaces 1 and 2 to the normal load applied to them. In all cases, the same normal load of $W = 590$ N/mm was applied so Figures 3.17, 3.18, and 3.19 show the differences in the friction force generated under different operating conditions and surface roughness profiles. In general, the friction force can be calculated via surface area integral as

$$f = \int_{A_s} \tau dS$$

As before, it is clear that the ground surface results in the most asperity interaction as indicated by the elevated χ_W; accordingly, the amount of asperity interaction decreases as

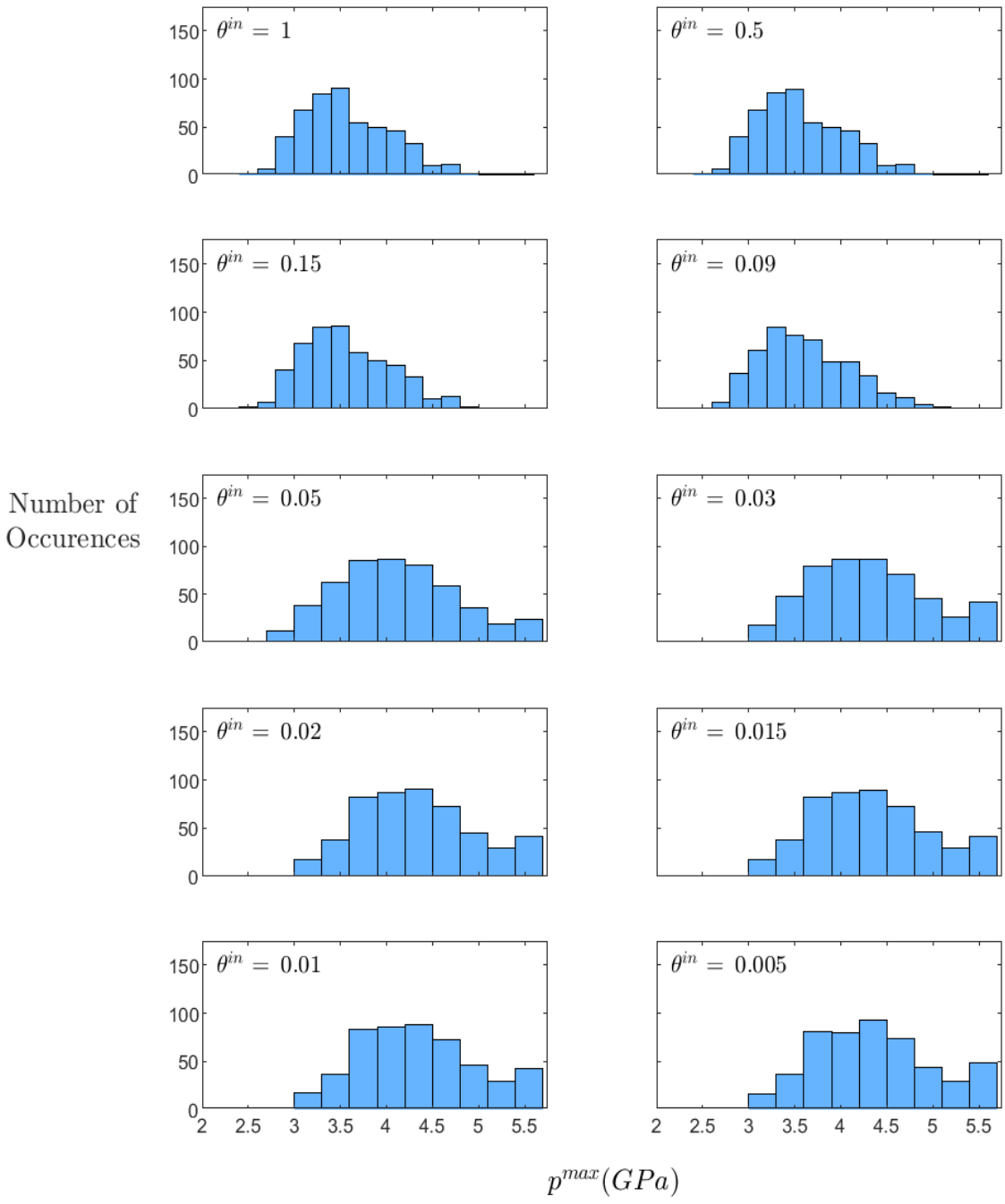

Figure 3.10: Probability density distribution of p^{max} for all film fraction boundary conditions under operating conditions $u_r = 15$ m/s, $SR = -1$, and the ground surface.

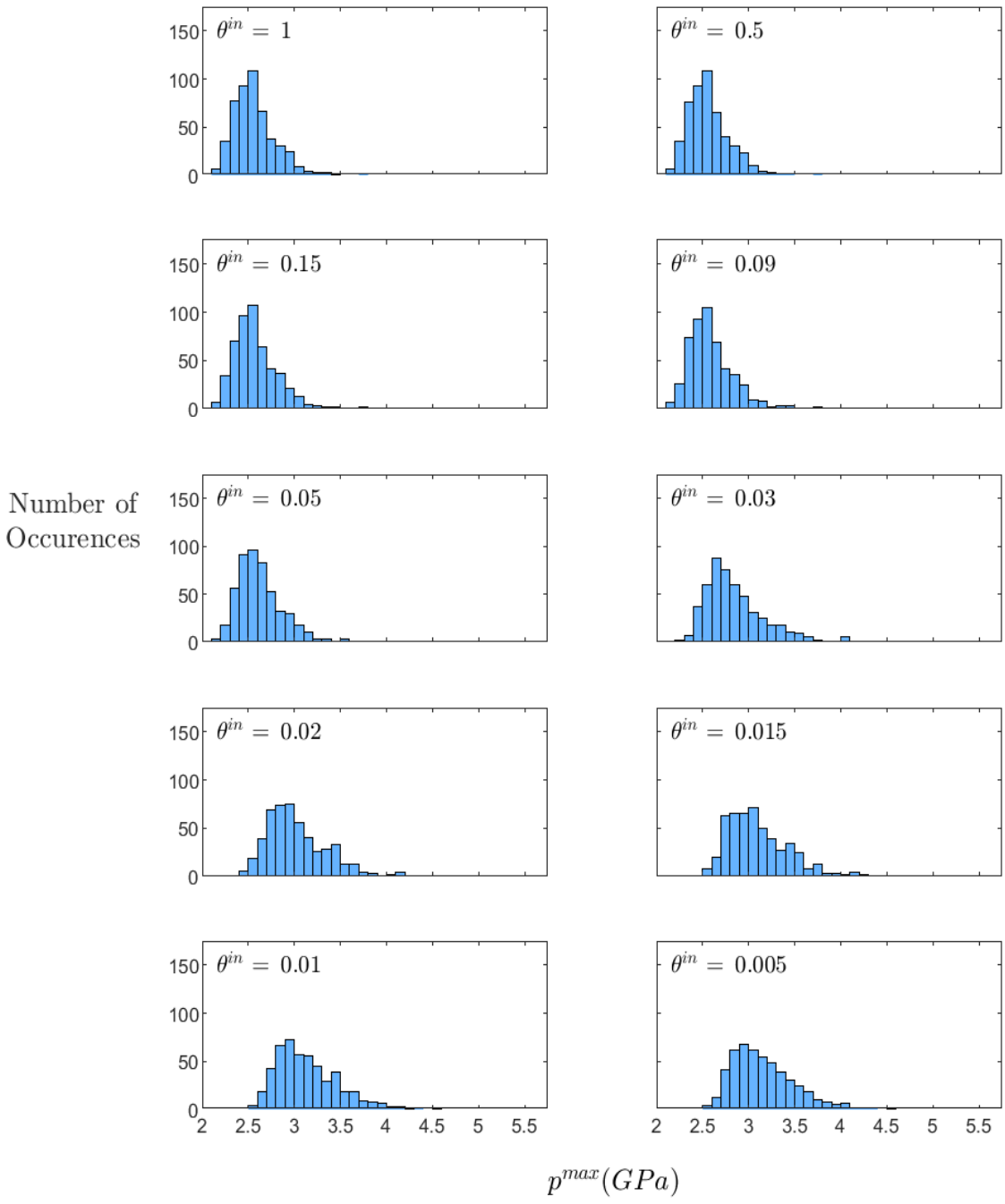

Figure 3.11: Probability density distribution of p^{max} for all film fraction boundary conditions under operating conditions $u_r = 15$ m/s, $SR = -1$, and the polished surface.

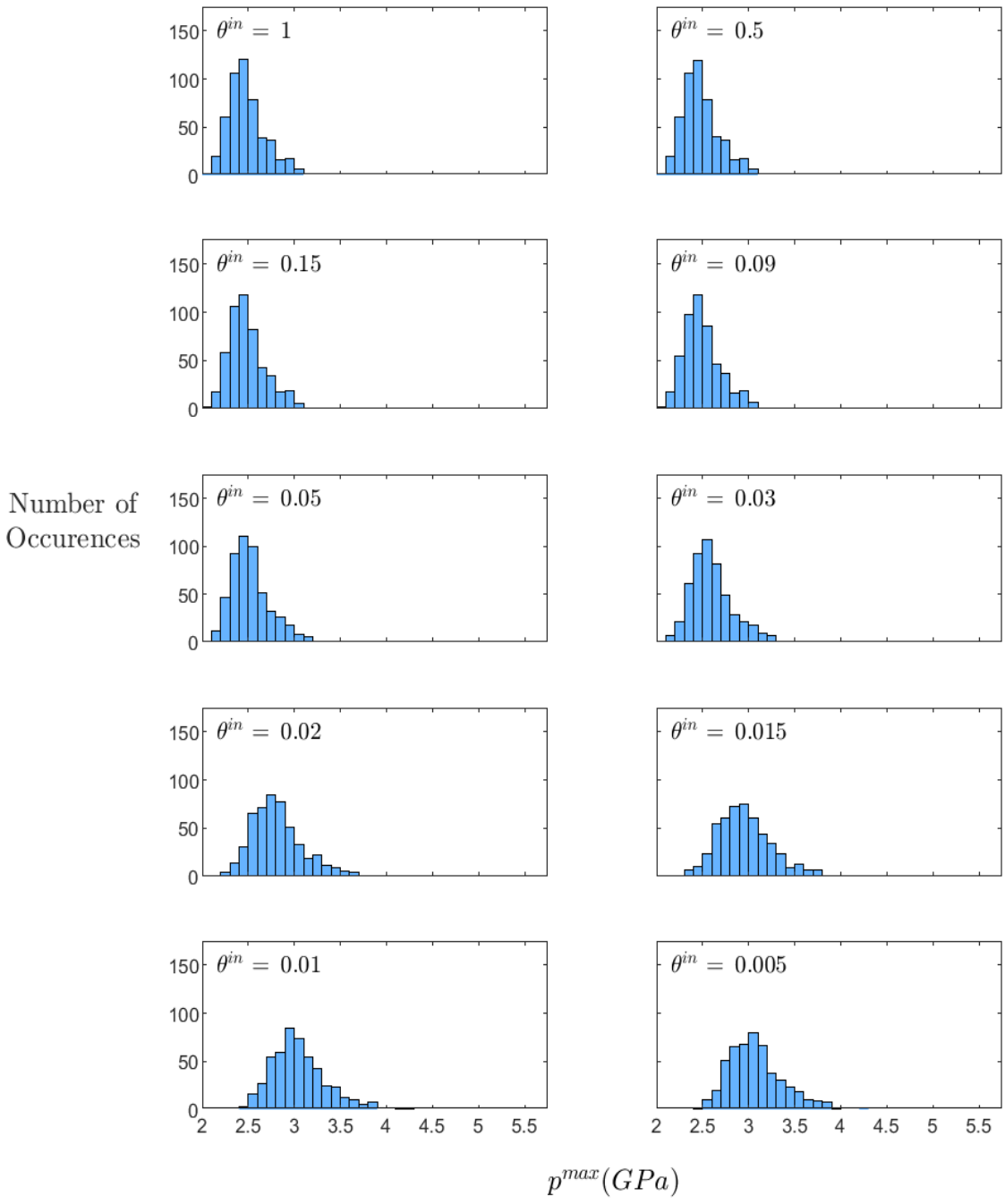

Figure 3.12: Probability density distribution of p^{max} for all film fraction boundary conditions under operating conditions $u_r = 15$ m/s, $SR = -1$, and the highly polished surface.

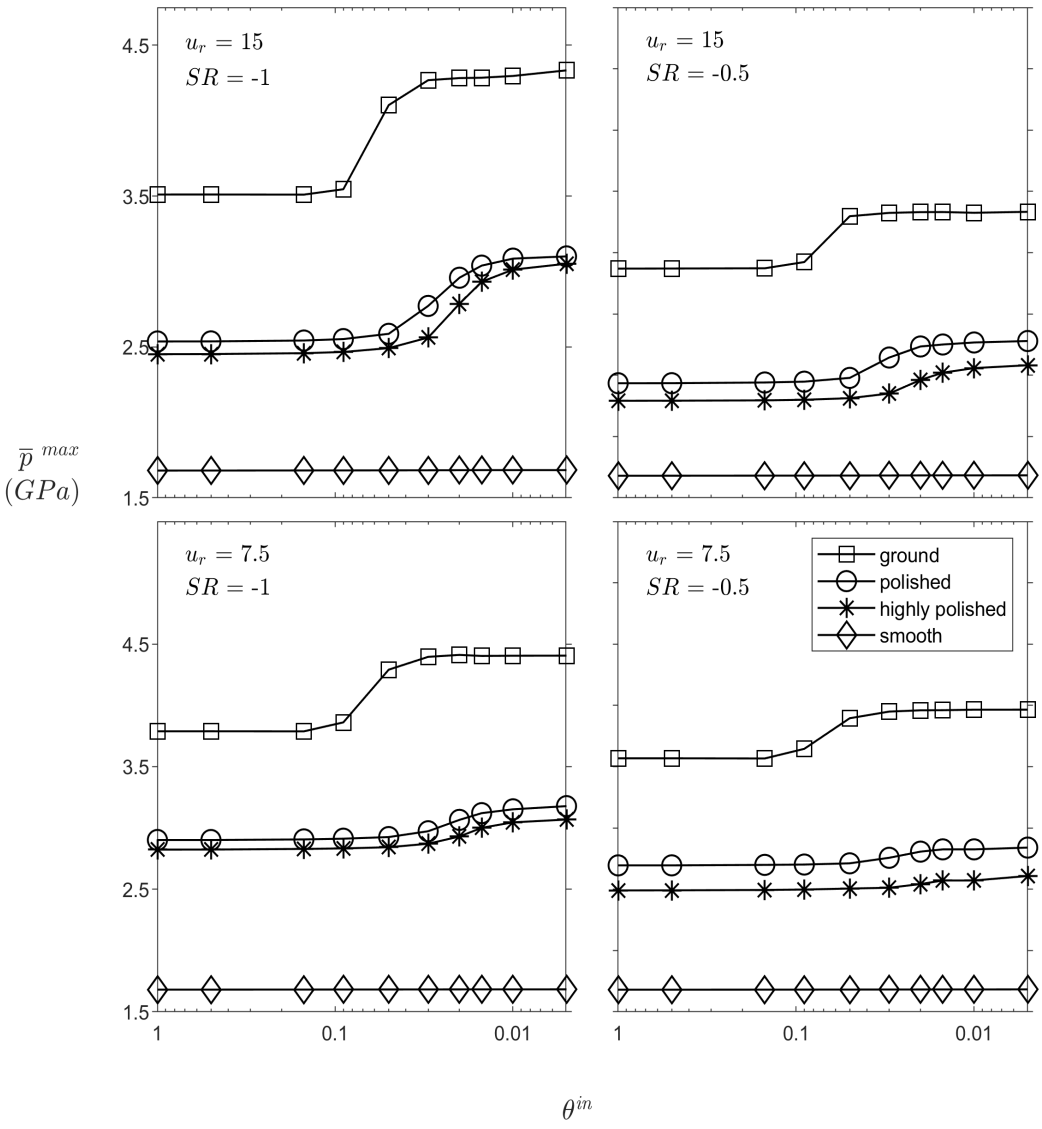

Figure 3.13: Variations of median maximum contact pressure with θ^{in} under various operating conditions.

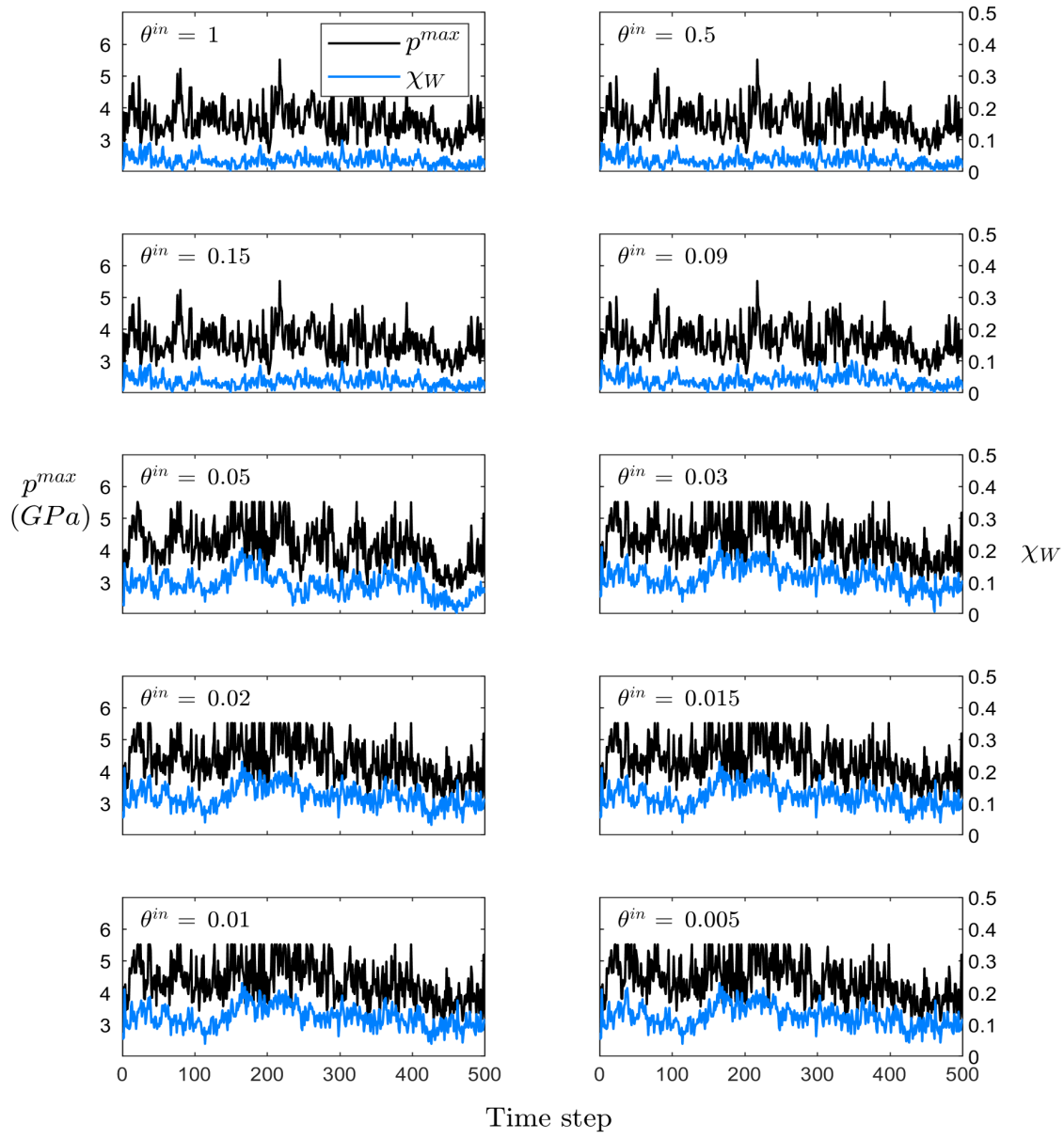

Figure 3.14: Variations of maximum contact pressure with χ_W for all film fraction boundary conditions under operating conditions $u_r = 15$ m/s, $SR = -1$, and the ground surface.

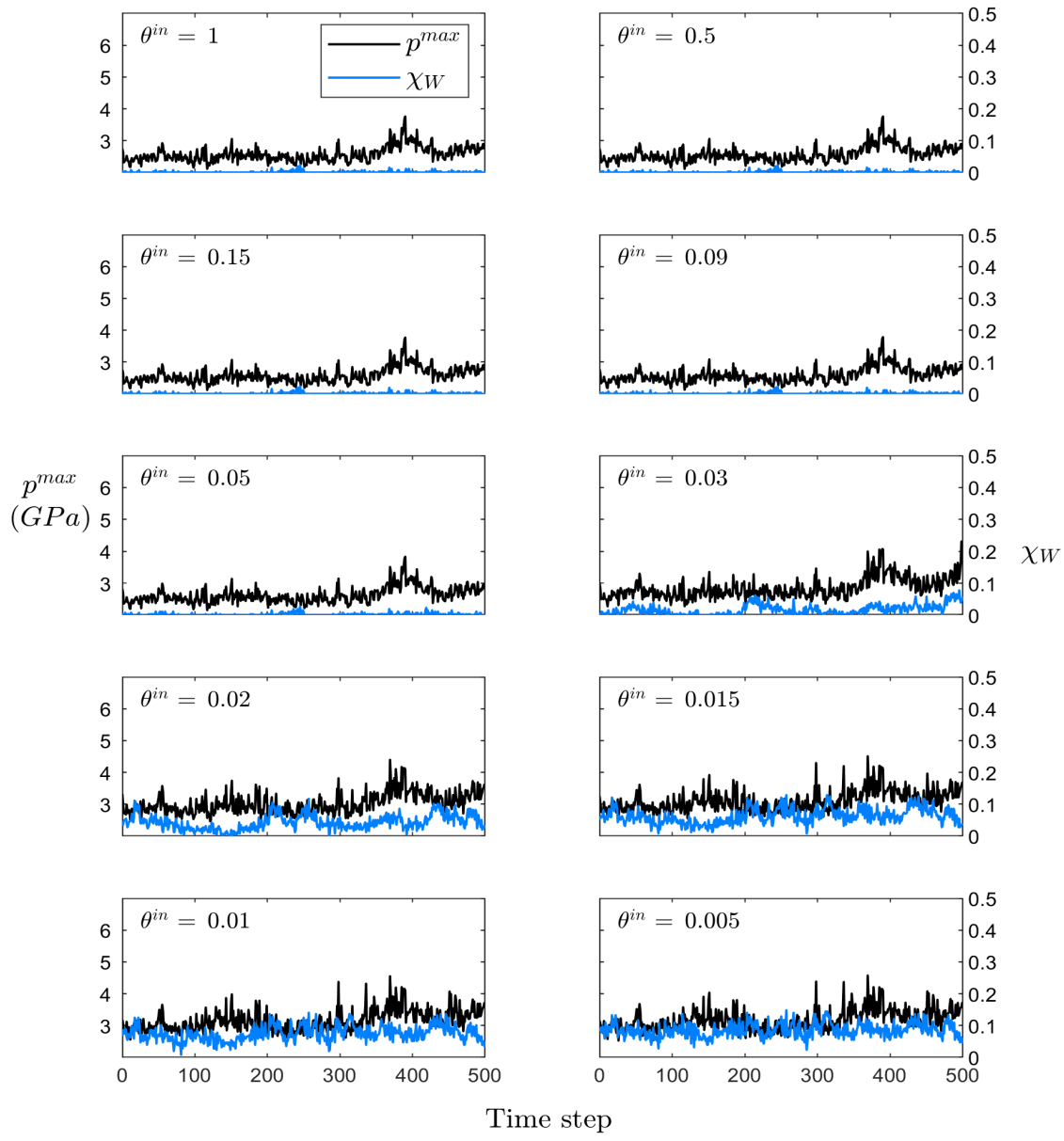

Figure 3.15: Variations of maximum contact pressure with χ_W for all film fraction boundary conditions under operating conditions $u_r = 15$ m/s, $SR = -1$, and the polished surface.

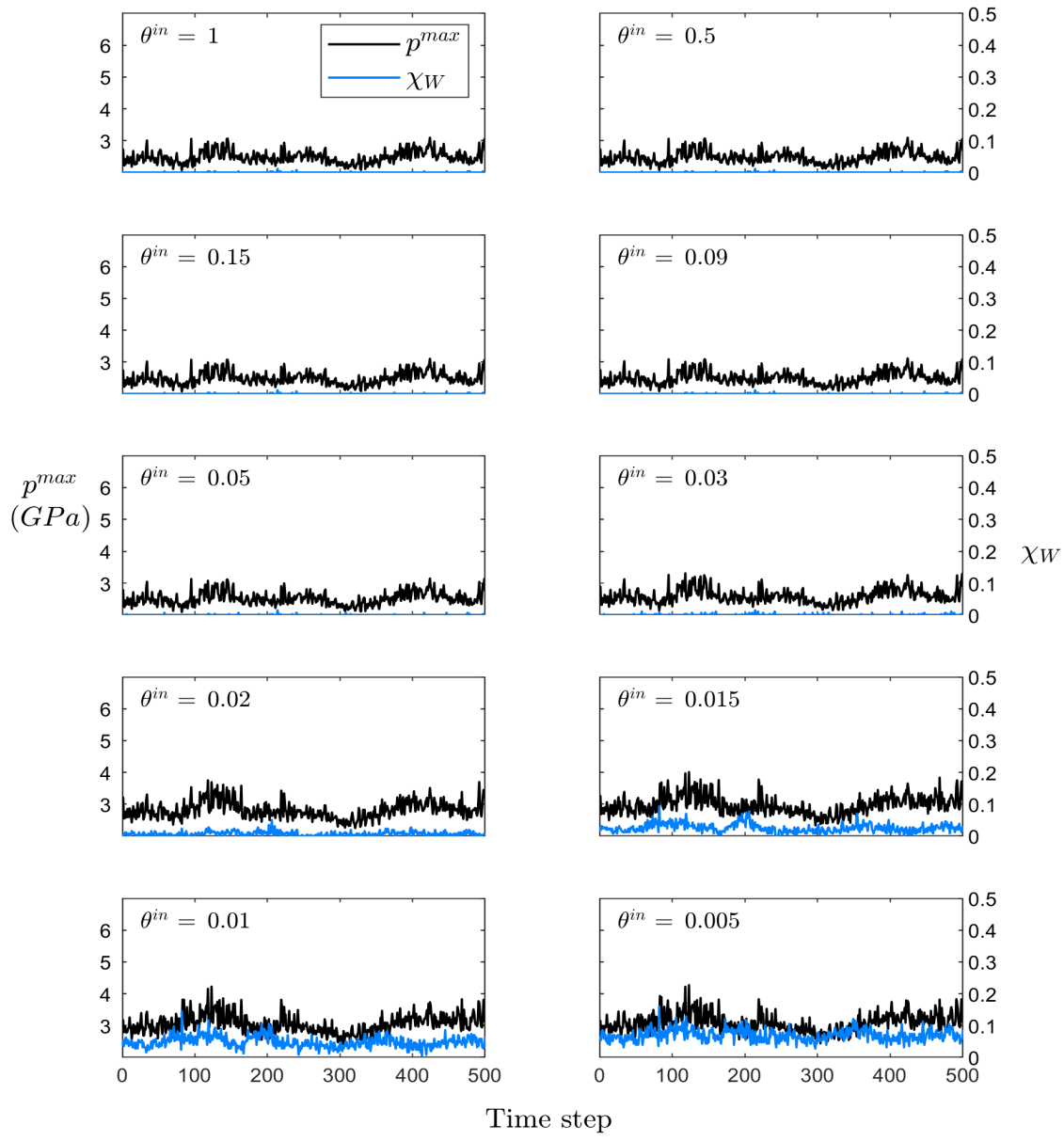

Figure 3.16: Variations of maximum contact pressure with χ_W for all film fraction boundary conditions under operating conditions $u_r = 15$ m/s, $SR = -1$, and the highly-polished surface.

the surface is made smoother by polishing. Since friction force originates from asperity interaction, the friction coefficient μ varies directly with χ_W in all cases. This is distinctly evident in Figure 3.17 where the plots of μ and χ_W with time have the same profile for all lubrication starvation conditions, with both quantities increasing as the starvation severity is increased. In Figures 3.18 and 3.19, the same behavior is observed but the magnitude of both μ and χ_W are decreased due to the smoother surfaces.

Similarly to the analysis of temperature and pressure, the median friction coefficient $\bar{\mu}$ was found and plotted for each possible combination of surface roughness profiles and operating conditions. This plot shows that for all operating conditions, the friction coefficient is lowest for the fully flooded lubrication condition and increases as the severity of the lubrication starvation is increased. It is also shown that for all operating conditions the three engineering surfaces arrive at very similar values of $\bar{\mu}$ for the most starved condition. Generally, the ground surface is shown to have the most dramatic increase in $\bar{\mu}$ and remains elevated above the values of $\bar{\mu}$ corresponding to all of the other engineering surfaces. An interesting trend which was not evident in similar plots of flash temperature and pressure is the elevation of $\bar{\mu}$ in the cases with lower magnitude sliding velocity. Since this holds for both values of u_r and $SR = \frac{u_s}{u_r}$, this indicates that increasing the sliding velocity u_s results in an increase in the friction coefficient μ. This is supported by Figure 3.21 which shows that μ is elevated in all starvation cases for the ground surface with u_r = 15 m/s, $SR = -0.5$ as compared to Figure 3.17 where the only difference is in the operating condition $SR = -1$. This increase in μ for the cases with $SR = -0.5$ are a result of the more balanced surface velocities for these cases as shown by Table 2.2. When the slide-to-roll ratio is decreased in magnitude, which corresponds to "low sliding", the difference in the surface velocities u_1 and u_2 is smaller. This results in longer periods of more severe asperity interaction, as shown by comparing Figures 3.17 and 3.21, which leads to increased friction force generated between the surfaces and thus higher friction coefficient.

3.5 Effects of Starvation on Power Loss

The power loss due to sliding between the solid surfaces can be calculated simply as:

$$P = fu_s$$

Following the previous analysis, the plots of power loss P for all lubrication conditions under the high velocity, high sliding operating conditions are shown in Figures 3.22, 3.23, and 3.24 for the ground, polished, and highly polished surface roughness profiles respectively. Figure 3.22 shows that the power loss varies proportionally with the amount of asperity interaction, and increases as the lubrication starvation is increased. Comparing this with Figures 3.23 and 3.24, it is clear that the power loss has the greatest magnitude and amount of variation for the ground surface and both of the characteristics decrease accordingly with the surface roughness.

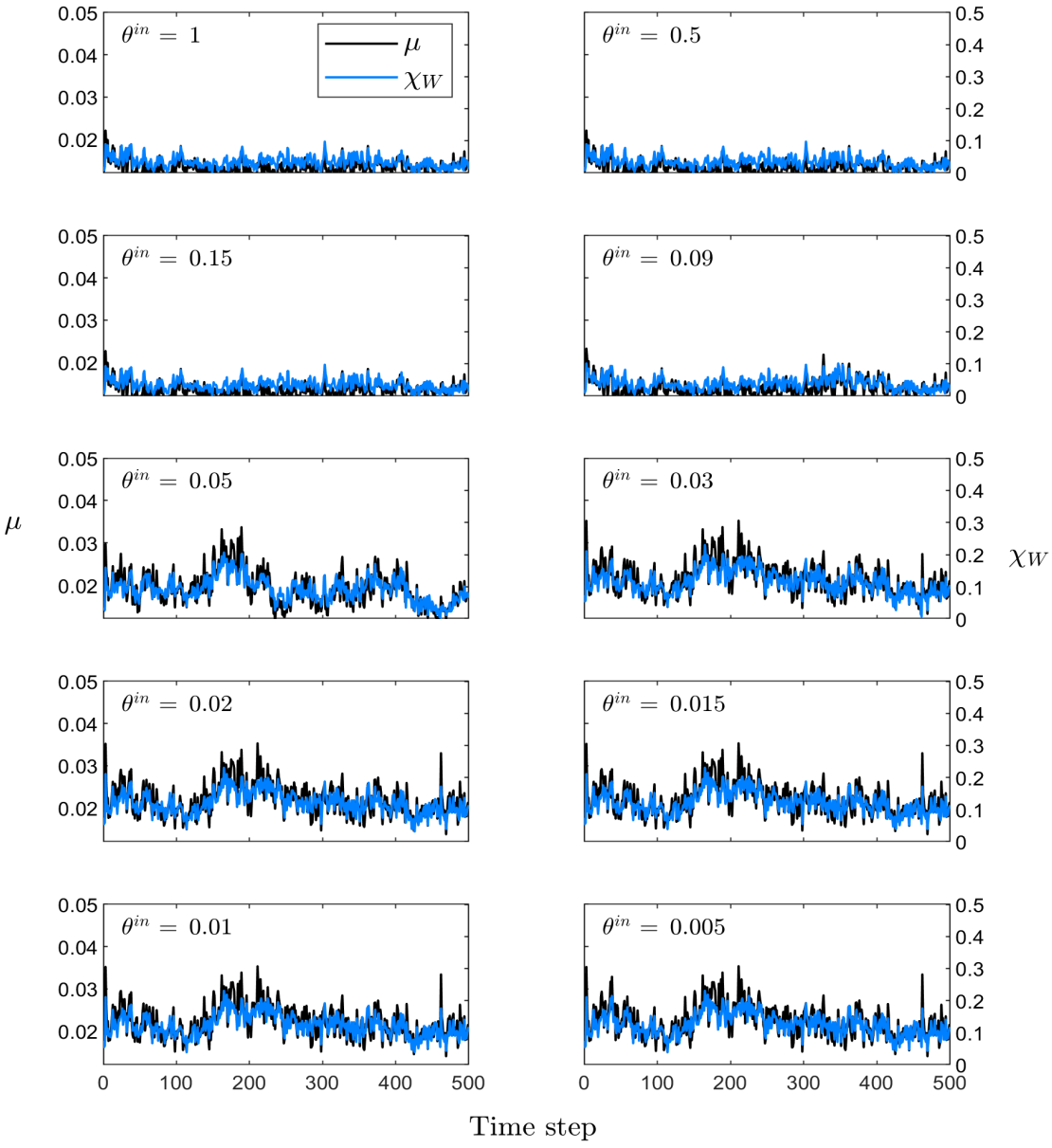

Figure 3.17: Variations of friction coefficient with χ_W for all film fraction boundary conditions under operating conditions $u_r = 15$ m/s, $SR = -1$, and the ground surface.

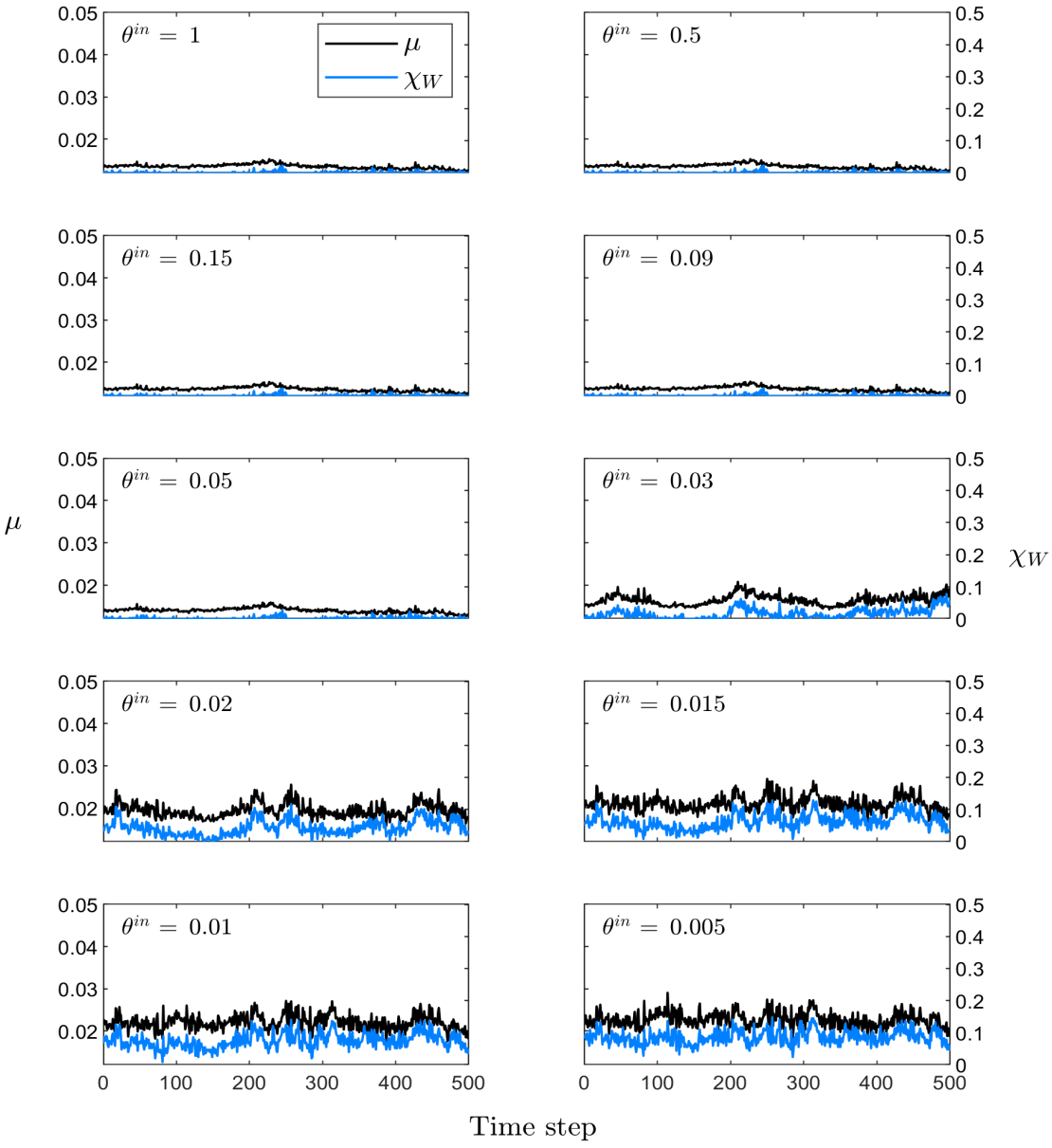

Figure 3.18: Variations of friction coefficient with χ_W for all film fraction boundary conditions under operating conditions $u_r = 15$ m/s, $SR = -1$, and the polished surface.

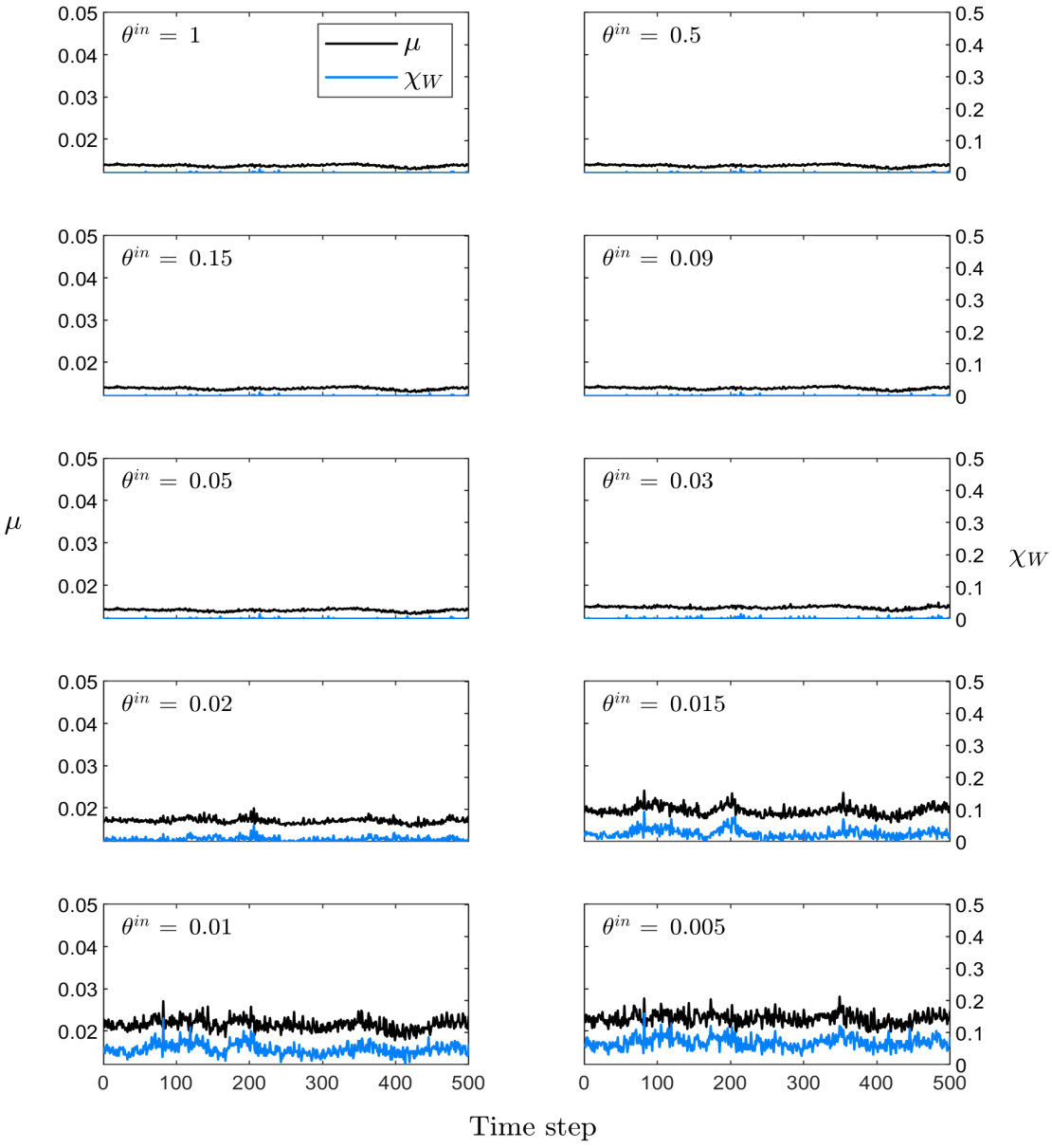

Figure 3.19: Variations of friction coefficient with χ_W for all film fraction boundary conditions under operating conditions $u_r = 15$ m/s, $SR = -1$, and the highly-polished surface.

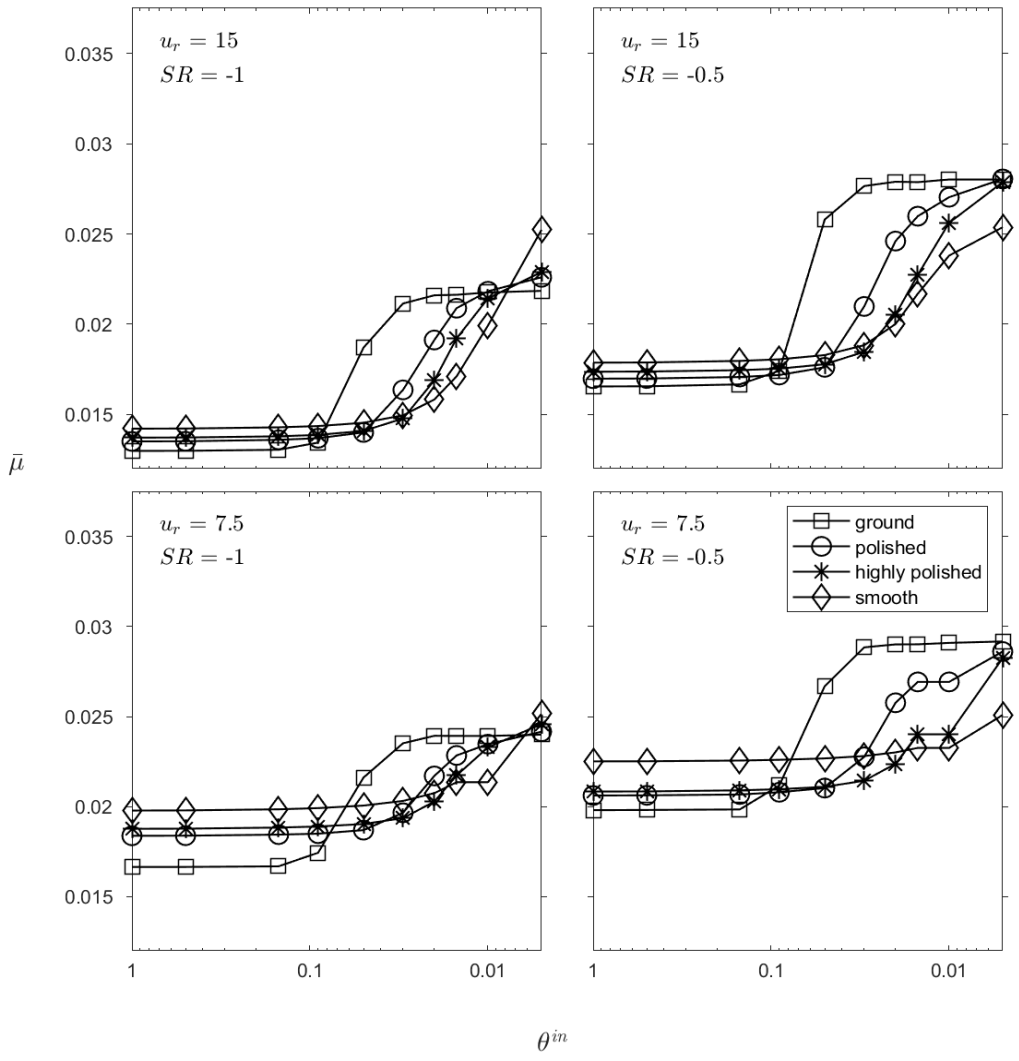

Figure 3.20: Variations of median friction coefficient with θ^{in} under various operating conditions.

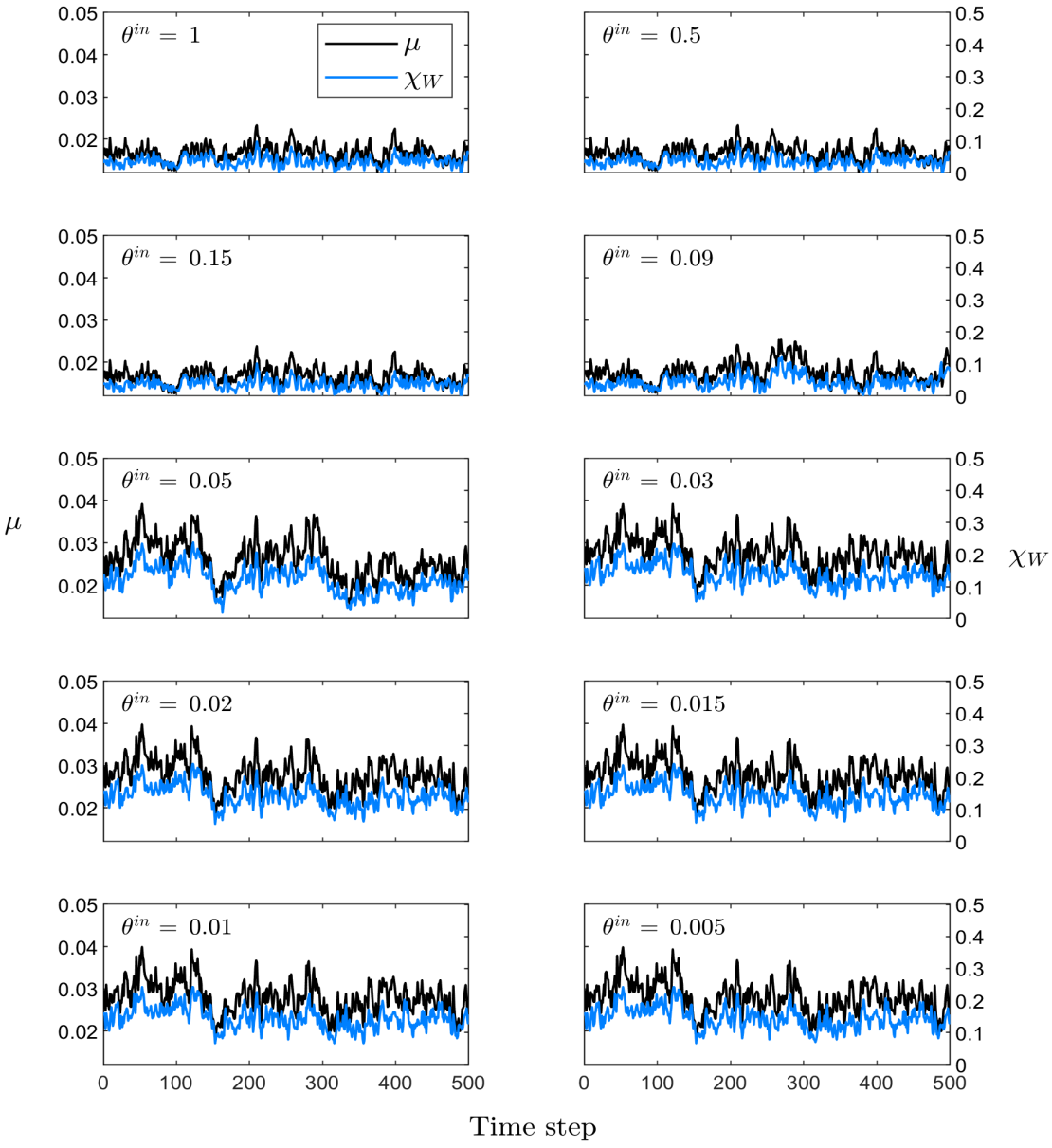

Figure 3.21: Variations of friction coefficient with χ_W for all film fraction boundary conditions under operating conditions $u_r = 15$ m/s, $SR = -0.5$, and the ground surface.

The median power loss for all surface roughness profiles under all operating conditions is shown in Figure 3.25. Here, it is clear that the high velocity, high sliding operating conditions produce the most power loss with the highest overall occurring for the ground surface. There is less variation between the surface loss of different surfaces for the cases with lower rolling velocities (bottom row). This indicates that a higher rolling velocity, which by definition means a higher average of the surface velocities, creates conditions which are more strongly influenced by asperity interaction. Since in the previous section it was discussed that the highest friction force is actually generated in the cases with lower slide-to-roll ratios, the highest power loss corresponding to the high velocity, high sliding case must be due to it having the largest magnitude rolling and sliding velocities.

3.6 Analysis of Single Time Instant

Considering that a great deal of the results discussed were produced by time-series analysis, it was also important to investigate the tribological behavior for one time instant with respect to spatial variations. In order to give an overarching view, the distributions of pressure, film thickness, temperatures (of surfaces 1 and 2 as well as the average fluid temperatures), and the film fraction parameter are shown for one time instant and the ground, polished, and highly-polished surfaces in Figures 3.26, 3.27, and 3.28 respectively. Each of these plots are for the highest sliding operating conditions of $u_r = 15$ m/s and $SR = -1$. It was previously shown that as the lubricant starvation severity is increased, so is the asperity interaction. This is supported by the elevated contact pressure shown in Figure 3.26 for the most severely starved case (top right subplot) as compared to the fully flooded condition (top left subplot). The elevated contact pressure results in the increase in fluid temperature as well as the temperatures of each solid surface as shown by the right middle subplot.

Recall that the film fraction parameter θ represents the mass content fluctuation due to changes in pressure which cause slight compression of the fluid. When θ^{in} = 1, the film fraction parameter θ maintains a value of 1 until the outlet cavitation occurs. As θ^{in} is reduced to introduce the starved lubrication condition, Figure 3.26 shows that θ increases slowly in the inlet zone and within the nominal Hertzian zone frequently drops to very small values indicating severe local cavitation. For the other engineering surfaces, the instantaneous distributions of the polished and highly polished surfaces are shown in Figures 3.27 and 3.28 respectively. These two smoother surfaces show that fully flooded lubrication is replaced by mixed lubrication as θ^{in} is reduced, increasing the contact pressures as well as lubricant and surface temperatures. The plots of θ for these smoother surfaces show that although there is local cavitation occurring in the nominal Hertzian zone indicated by θ falling below 1, the occurrence is less frequent than for the ground surface and the values of θ are not as small. Comparing the top rows of Figures 3.26, 3.27, and 3.28, it is clear that the film thickness for the ground surface profile is the largest due to it having the most significant surface roughness fluctuations. When these surface roughness fluctuations are reduced via polishing, the film thickness decreased accordingly; this is due to

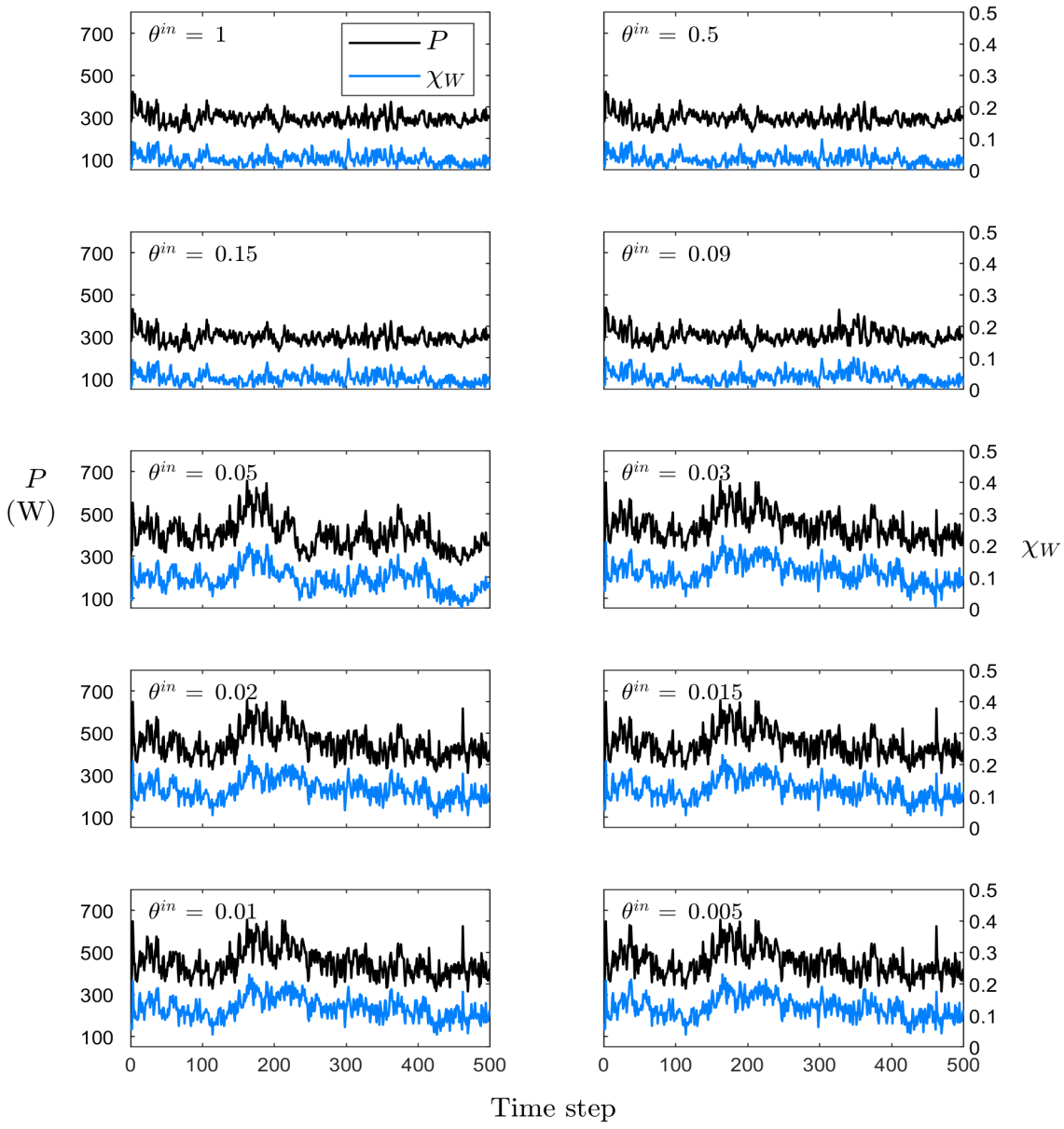

Figure 3.22: Variations of power loss with χ_W for all film fraction boundary conditions under operating conditions $u_r = 15$ m/s, $SR = -1$, and the ground surface.

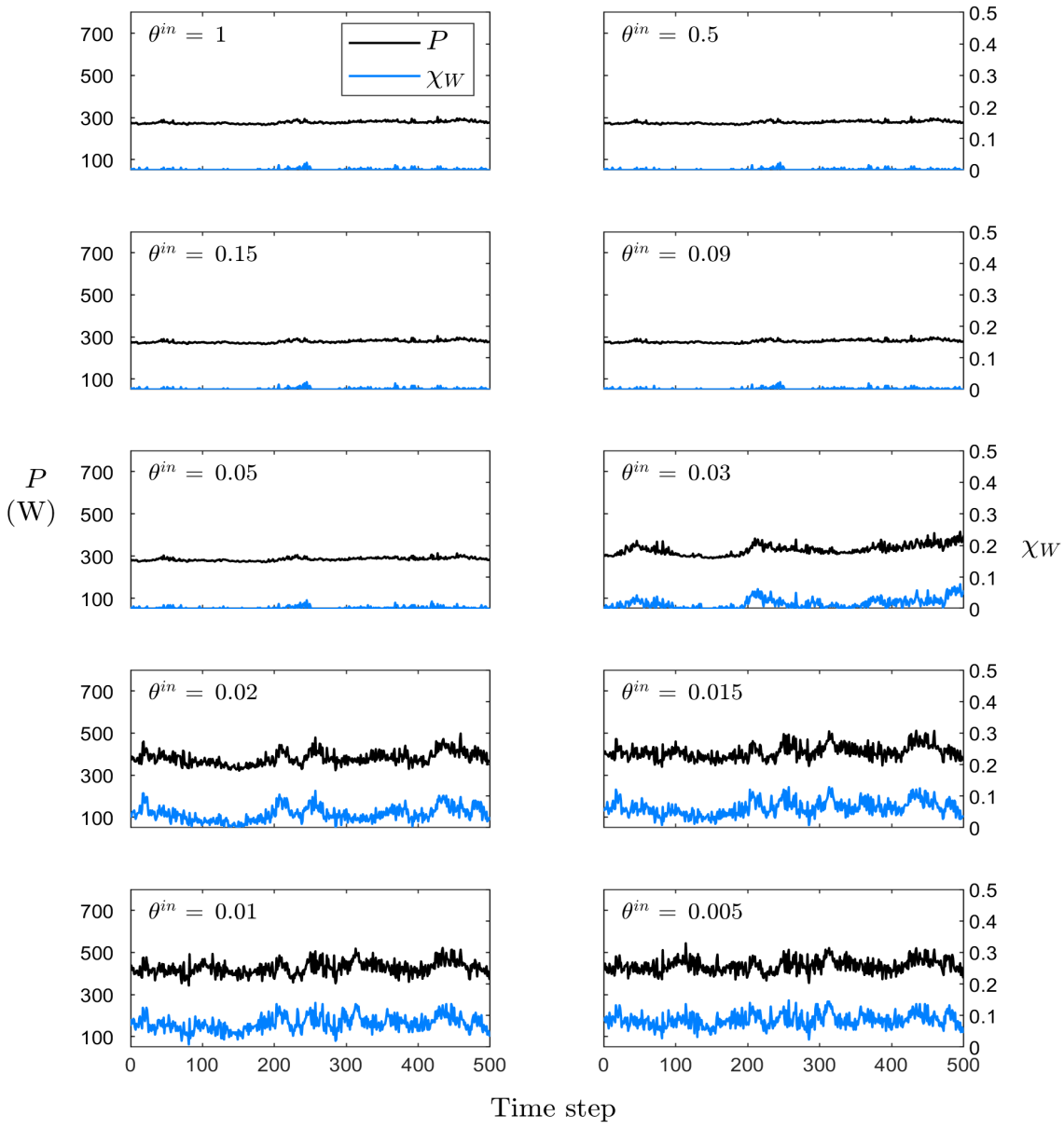

Figure 3.23: Variations of power loss with χ_W for all film fraction boundary conditions under operating conditions $u_r = 15$ m/s, $SR = -1$, and the polished surface.

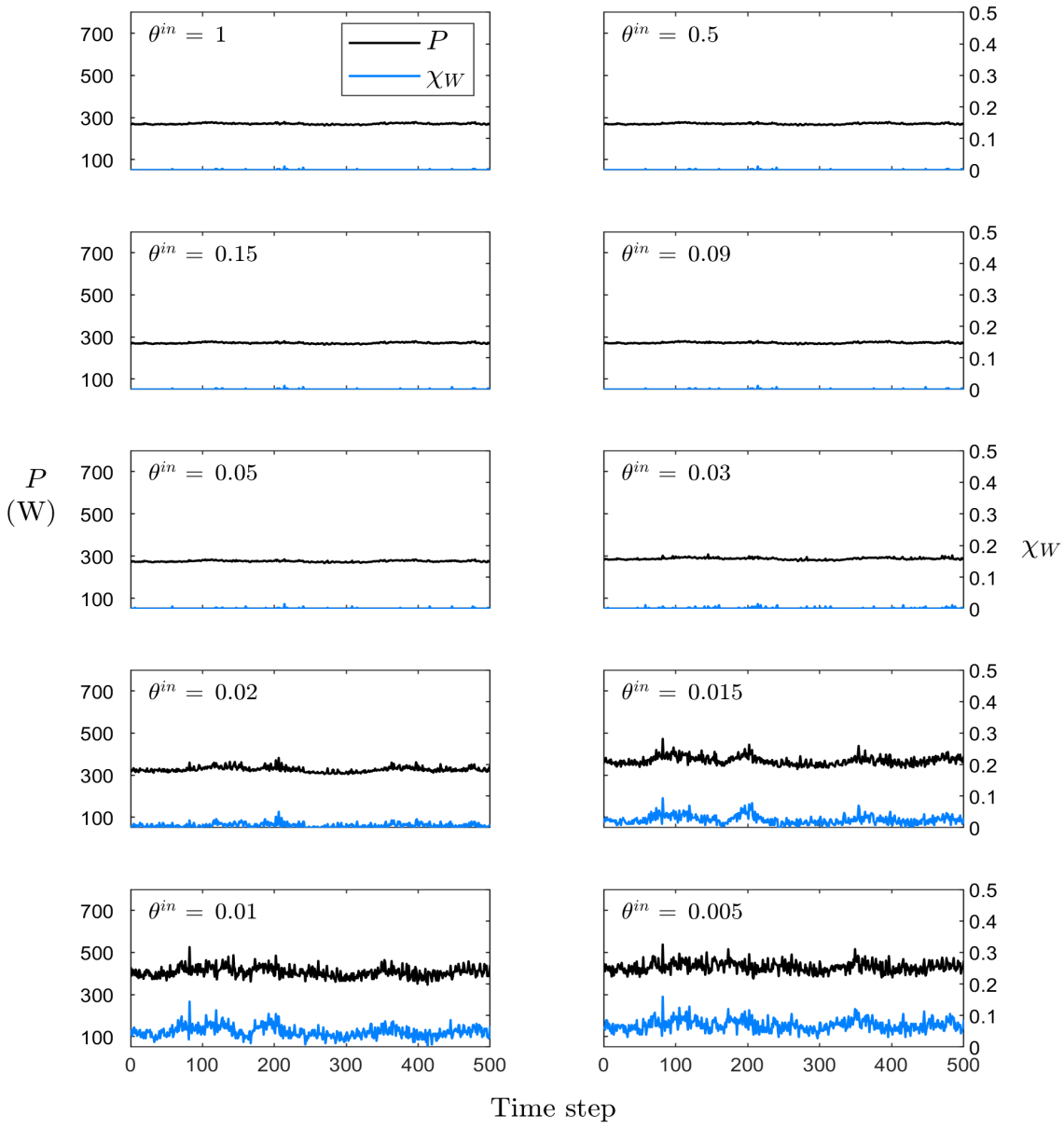

Figure 3.24: Variations of power loss with χ_W for all film fraction boundary conditions under operating conditions $u_r = 15$ m/s, $SR = -1$, and the highly-polished surface.

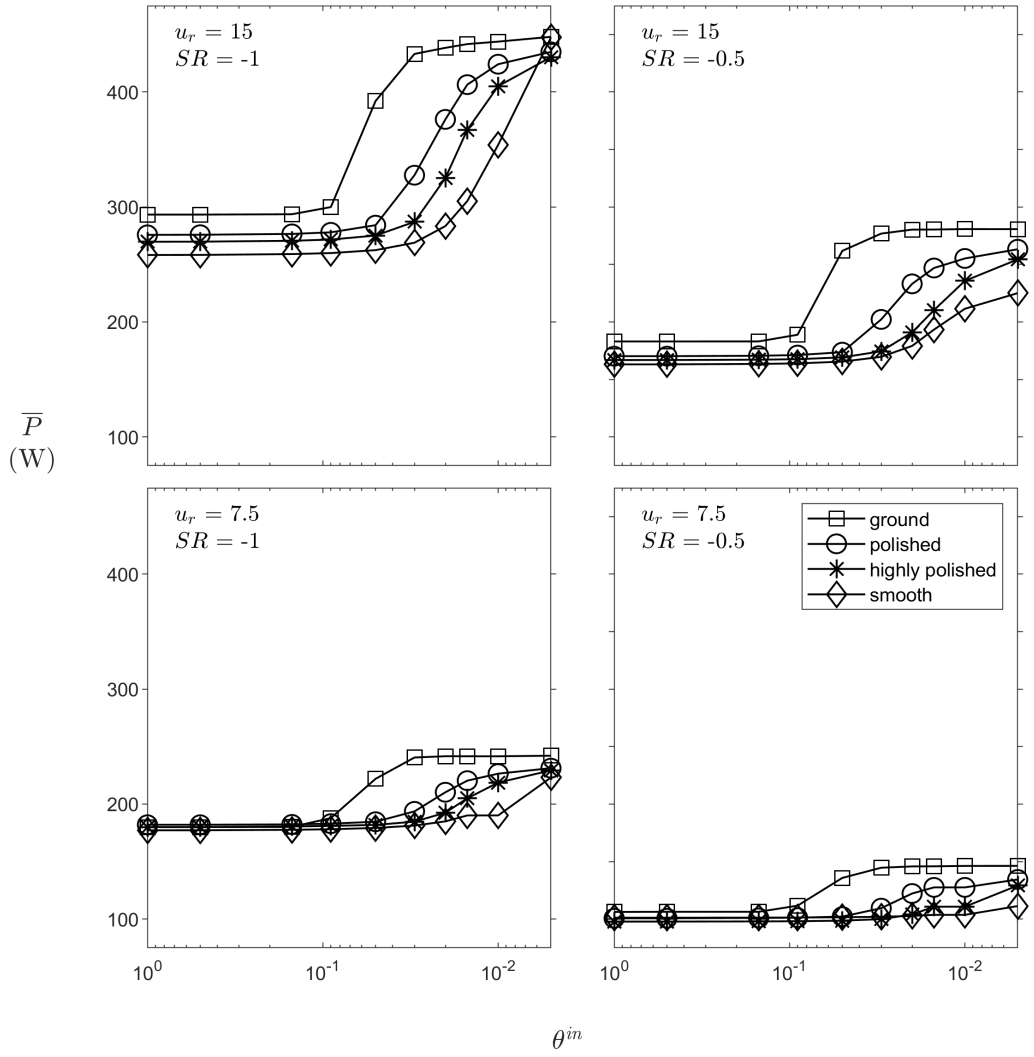

Figure 3.25: Variations of median power loss with θ^{in} under various operating conditions.

the equilibrium condition between the contact pressure and the applied normal force, i.e. $W = \int pdx$, which allows the two surfaces with reduced surface roughness to come closer together without producing excessive contact pressure.

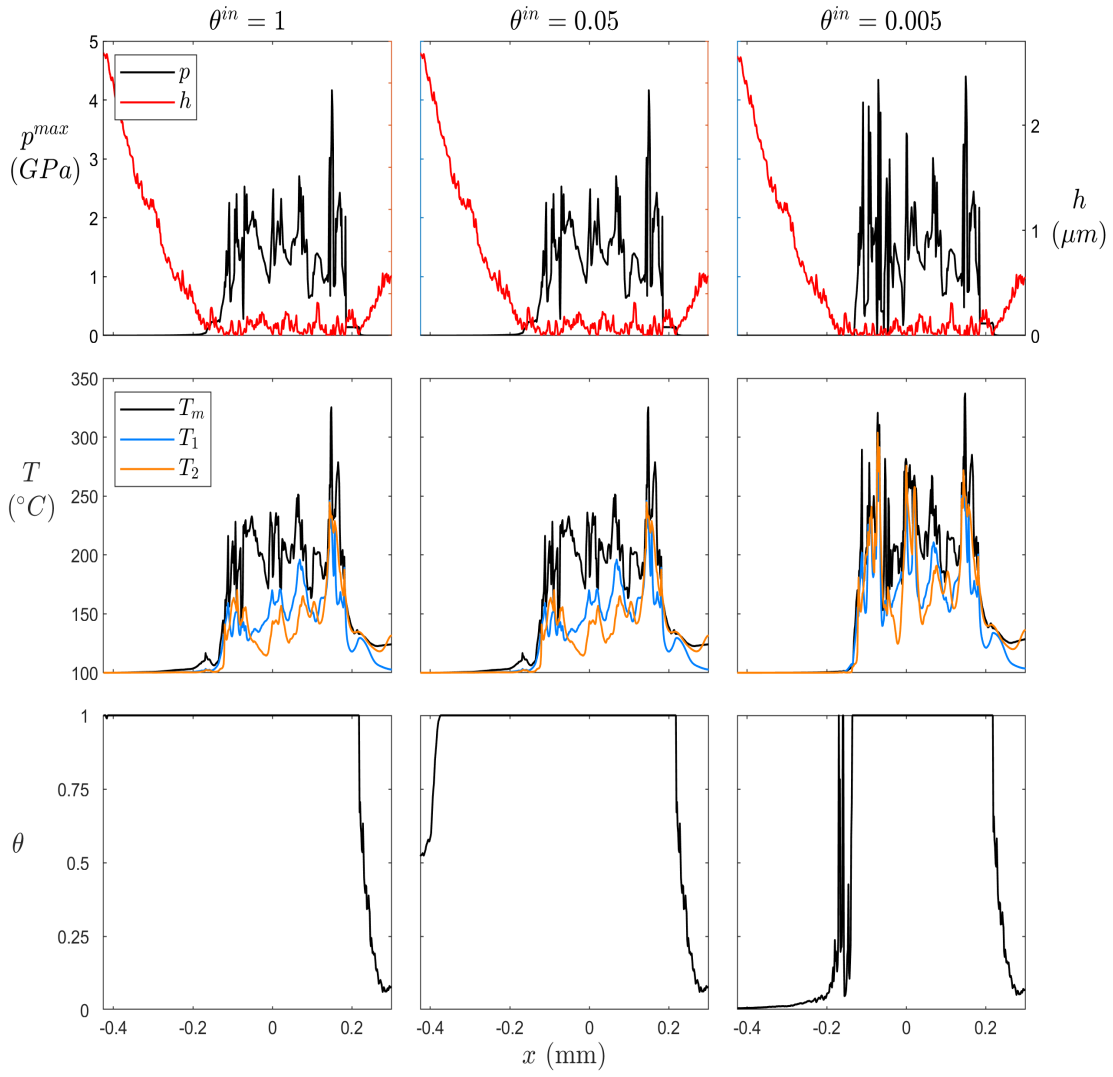

Figure 3.26: The distributions of pressure and film thickness (top), temperature (middle), and film fraction (bottom) at one time instant for the ground surface operating under $u_r = 15$ m/s and $SR = -1$. The left, middle, and right columns correspond to θ^{in} = 1, 0.5, and 0.05 respectively.

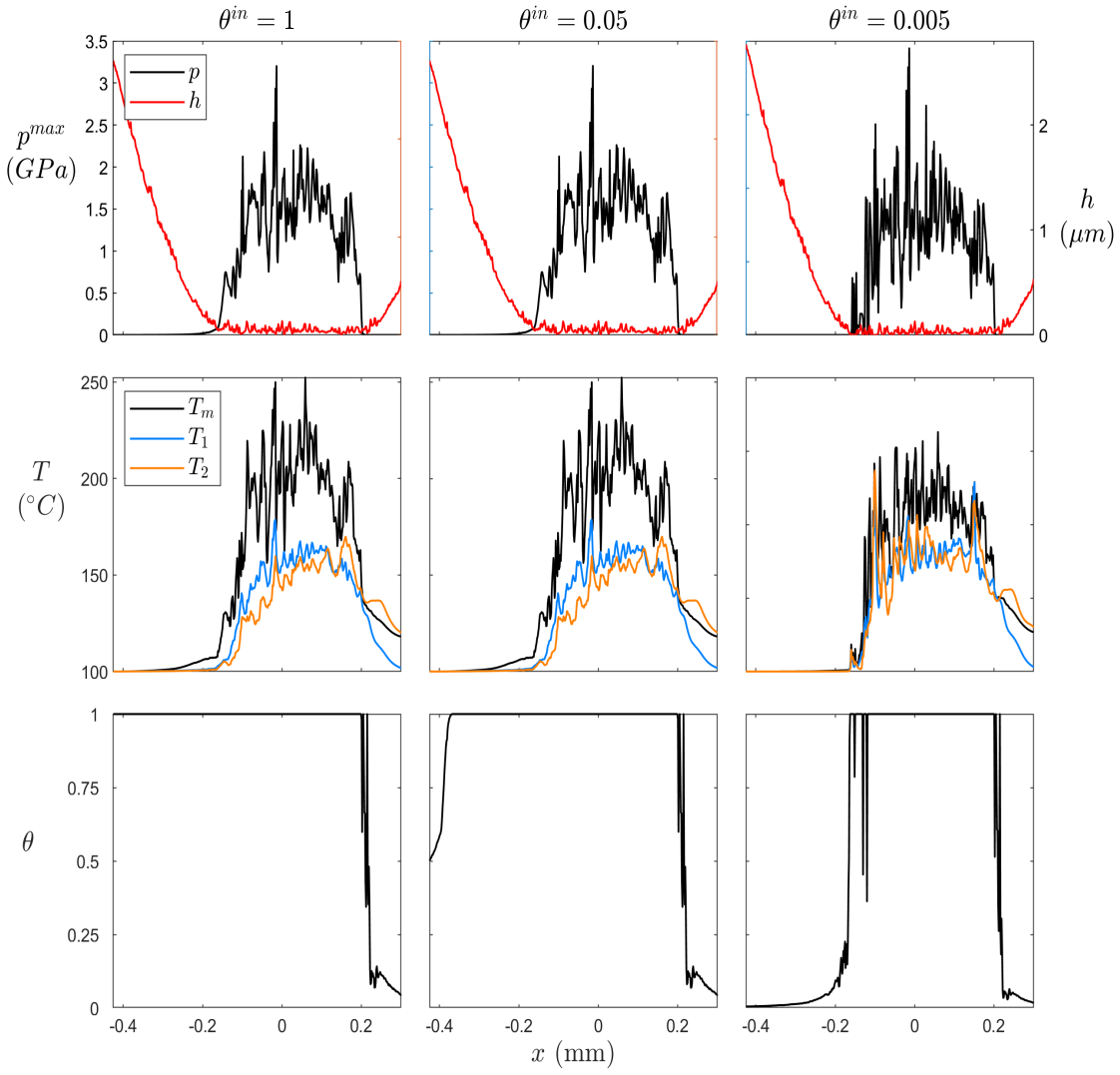

Figure 3.27: The distributions of pressure and film thickness (top), temperature (middle), and film fraction (bottom) at one time instant for the polished surface operating under $u_r = 15$ m/s and $SR = -1$. The left, middle, and right columns correspond to θ^{in} = 1, 0.5, and 0.05 respectively.

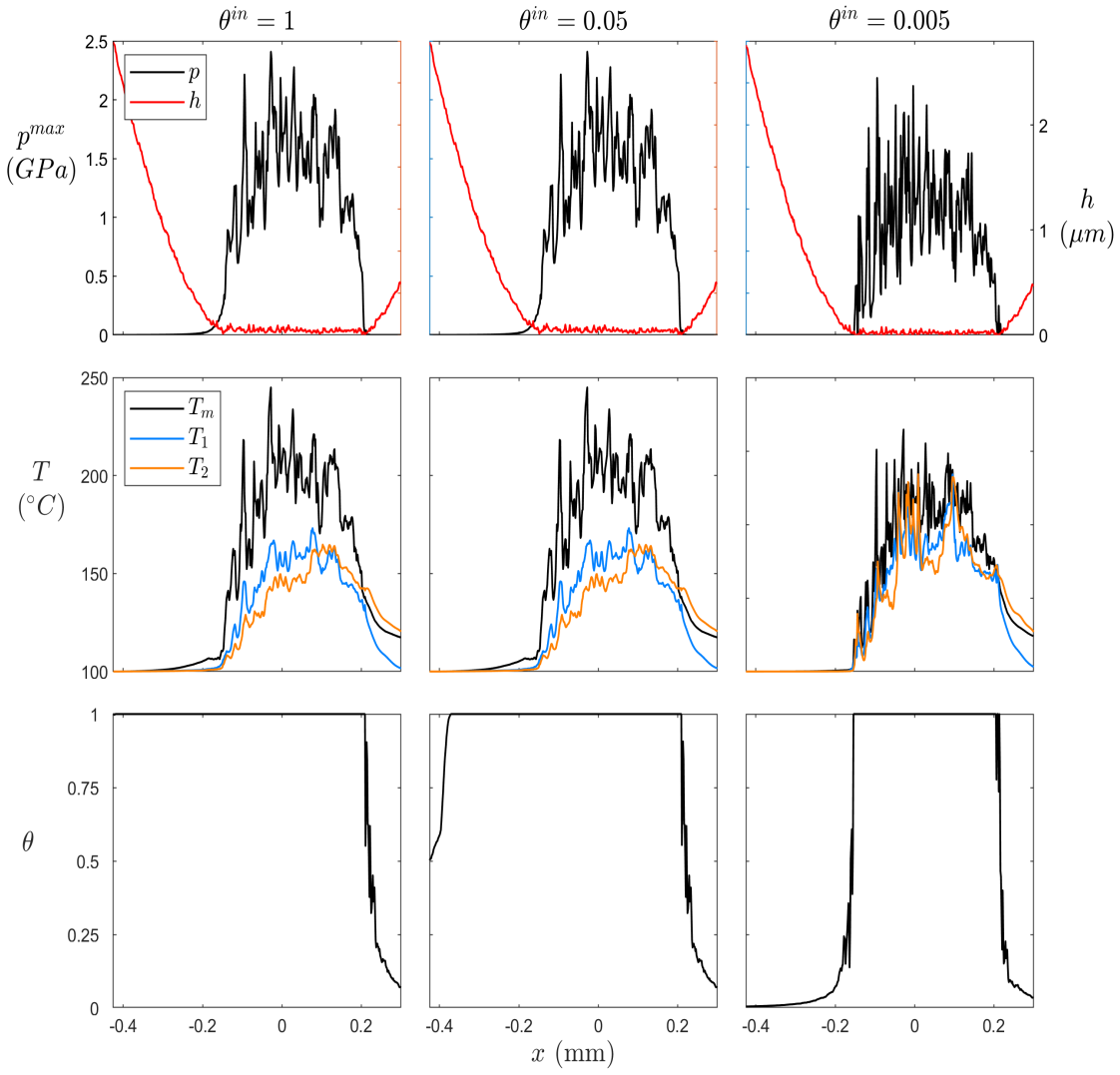

Figure 3.28: The distributions of pressure and film thickness (top), temperature (middle), and film fraction (bottom) at one time instant for the highly-polished surface operating under $u_r = 15$ m/s and $SR = -1$. The left, middle, and right columns correspond to θ^{in} = 1, 0.5, and 0.05 respectively.

Summary and Conclusion

4.1 Summary

This thesis presents a parametric study of the effects of lubrication starvation on a spur gear line contact via numerical simulation. The overall goal of this work is to computationally examine the effects of lubrication starvation and high speed operating conditions on the flash temperature of the contact surfaces, and to draw conclusions about the likelihood of scuffing failure in the different scenarios considered. The first challenge in developing this work lies in understanding the numerical approach.

In order to accurately account for the mass content fluctuations that occur with changes in the pressure, the θ approach taken in [48] is used. The variable of highest interest in these simulations is the flash temperature on the surface of the contact. This is found by further implementing a heat transfer model between the lubricant and contact surfaces which accounts for conductive heat transfer across the fluid film, the work done on the lubricant by viscous forces, the net outflow of thermal and internal energy in the rolling direction, and the rate of storage of internal energy. Realistic models are used for all major physical characteristics of the lubricant. All simulations were conducted for lubricant flow modeled by the generalized Newtonian Reynolds equation, with the non-Newtonian behavior of the lubricant included through the flow coefficient which utilizes a modified Carreau model. The compressibility of the lubricant is taken into account by an approximate formulation which includes dependencies of the density on both pressure and temperature; similarly, the viscosity also follows a pressure and temperature dependent model. Numerical convergence is reached by applying an equilibrium condition at each time step which demands that the load applied to the system be equal to the distributed pressure over the contact zone. Further, it is required that the pressure and temperatures approach a consistent value at each time step.

In addition to the numerical complexity of the line contact model presented here, the surface profiles of the contact surfaces are real. They were measured using a surface profiler, and in total four surfaces were used corresponding to three real gear tooth surfaces and one idealized (perfectly flat) surface. The three engineering surfaces used correspond

to different levels of polishing; overall, ground, polished, and highly polished surfaces were used with the ground surface begin the roughest, i.e. having the most variation. Each surface was subjected to different operating and starvation conditions.

The load applied was the same for all simulations - the operating conditions which varied were the rolling and sliding velocities, which together determine the velocities of the contact surfaces. Each velocity was given two different values, making 16 different combinations. The chosen values correspond to realistic operating conditions for spur gears in aerospace applications, a situation which is well-known to be particularly susceptible to scuffing failure.

The final complexity in this study is the lubrication starvation. The formulation was implemented intentionally such that knowledge of the inlet cavitation geometry was not necessary - instead, the severity of the starvation was able to be provided explicitly. In all, 10 different starvation levels were used to represent the range from fully-flooded lubrication conditions to an extremely starved situation, which is known to occur prior to scuffing failure when debris blocks the lubrication inlet. Hence, all told the results here correspond to 160 total tribological simulations.

4.2 Conclusions

Considering the results presented in Chapter 3, the following conclusions can be reached regarding the effects of lubrication starvation and high speed operating conditions on scuffing failure of spur gears:

- Flash temperatures of the same magnitude as those established in the literature as a criteria for the occurrence of scuffing failure were observed for the ground surface under the high sliding and high rolling operating conditions for lubrication starvation $\geq 50\%$.
- As the severity of lubrication starvation is increased, it is observed that:
  - the median maximum surface temperature increases
  - the amount of asperity interaction increases
  - the median average film thickness decreases
  - the median maximum contact pressure increases
  - the friction coefficient increases
  - the median power loss increases

  Overall this suggests that as the lubrication starvation severity is increased, the operation becomes less efficient in terms of power loss and increased frictional heating, which is the mechanism that leads to the occurrence of scuffing failure. Hence, spur

gears subjected to starved lubrication are more likely to experience scuffing failure, with extreme starvation corresponding to the highest chances.

- Under the high sliding and high rolling operating conditions, it is observed that:
  - the median maximum surface temperature is maximal for all engineering surface profiles
  - the median average film thickness is slightly elevated
  - the median maximum contact pressure is maximal for all engineering surface profiles; it is especially elevated in the high sliding cases
  - the median friction coefficient is minimal for all engineering surface profiles
  - the median power loss is maximal for all engineering surface profiles

  These results suggest that operating at high velocities (rolling and sliding) lead to tribological conditions which are most susceptible to scuffing failure. This supports the observation of such failures in industrial applications, and further provides evidence that spur gears under high speed operating conditions - particularly high sliding conditions - require special considerations considering the higher likelihood of scuffing failure.

- As the RMS roughness amplitude is decreased, it is observed that:
  - the median maximum surface temperature decreases
  - the median average film thickness decreases
  - the median maximum contact pressure decreases
  - the variation of the friction coefficient decreases
  - the median power loss decreases

  These results support using polishing compounds to mitigate the chances of scuffing failure since the highly polished surface was the least likely to experience high flash temperatures or marked increases in frictional heating.

4.3 Recommendations for Future Work

The numerical results presented here have offered a lot of information about the effects of lubrication starvation on gear contacts an their susceptibility to scuffing failure for realistic engineering surfaces under high speed operating conditions, with robust models used for all lubricant properties. Still, many aspects could be better understood with further numerical and experimental investigations.

In particular, a significant assumption is made in the heat transfer model concerning the boundary lubrication friction coefficient μ_b. For the results presented here, a constant

value of $\mu_b = 0.1$ was used which is reasonable for the boundary layer lubrication regime. However, it is well-known that the friction coefficient increases as the amount of lubrication decreases and so it is not certain whether the chosen constant friction coefficient is the most accurate for differing amounts of lubrication starvation. To increase the fidelity of the model, future work could focus on experimental characterization of different lubricants under a range of lubrication starvation severity and the results could then be incorporated into the computational model.

Bibliography

[1] ASTM International. *ASTM G40-17, Standard Terminology Relating to Wear and Erosion*. West Conshohocken, Pennsylvania, 2017.

[2] B. Bhushan. *Modern Tribology Handbook*. CRC Press, Boca Raton, FL, 2001.

[3] P. J. Blau. *Tribosystem analysis : a practical approach to the diagnosis of wear problems*. CRC Press, Boca Raton, Florida, 2016.

[4] P. J. Blau. *Scuffing: from basic understanding to engine materials testing*. DEER Conference, Detroit, Michigan, 2007.

[5] D. Arnell. *Tribology and dynamics of engine and powertrain: fundamentals, applications, and future trends*. Woodhead Publishing, Sawston, Cambridge, UK, 2016.

[6] A. R. Hassan. Contact stress analysis of spur gear teeth pair. *World Academy of Science, Engineering and Technology*, 58: 611–616, 2009.

[7] H. Blok. Theoretical study of temperature rise as surfaces of actual contact under oiliness lubricating conditions. *Proc. General Discussion on Lubrication and Lubricants (Proc. Inst. Mech. Engrs.)*, 2: 222–235, 1937.

[8] A. Dyson. The failure of elastohydrodynamic lubrication of circumferentially ground discs. *Proc. Inst. Mech. Engrs.*, 190: 52–76, 1976.

[9] J. C. Enthoven, P. M. Cann, and H. A. Spikes. Temeprature and scuffing. *Tribology Transactions*, 36 (2): 258–266, 1993.

[10] M. J. Patching, C. C. Kweh, H. P. Evans, and R. W. Snidle. Conditions for scuffing failure of ground and surperfinished steel disks at high sliding speeds using a gas turbine engine oil. *ASME Journal of Tribology*, pages 482–489.

[11] S. C. Lee and H. Chen. Experimental validation of critical temperature-pressure theory of scuffing. *Tribology Transactions*, 38 (3): 738–742, 1995.

[12] S. C. Lee and H. Chen. Correlation of scuffing experiments with ehl analysis of rough surfaces. *Journal of Tribology*, 133 (2): 318–326, 1991.

[13] S. C. Lee and H. Chen. Scuffing theory modeling and experimental correlations. *Journal of Tribology*, 113 (2): 327–334, 1991.

[14] J. C. Enthoven and H. A. Spikes. Visual observation of the process of scuffing. *Tribology Series, Lubricant and Lubrications - Proceedings of the 21st Leeds-Lyon Symposium on Tribology*, 30: 487–494, 1995.

[15] A. Jackson, M. N. Webster, and J. C. Enthoven. The effect of lubricant traction on scuffing. *Tribology Transactions*, 37 (2): 387–395, 1994.

[16] P. M. Ku. Gear failure modes - importance of lubrication and mechanics. *Tribology Transactions*, 19: 239–249, 1976.

[17] W. F. Bowman and G. W. Stachowiak. A review of scuffing models. *Tribology Letters*, pages 113–131, 1996.

[18] K. Ludema. A review of scuffing and running-in of lubricated surfaces, with asperities and oxides in perspective. *Wear*, 100: 315–331, 1984.

[19] S. Li, A. Kahraman, N. Anderson, and L.D. Wedeven. A model to predict scuffing failures of a ball-on-disk contact. *Tribology International*, 60: 223–245, 2013.

[20] S. Li. Influence of surface roughness lay directionality on scuffing failure of lubricated point contacts. *ASME Journal of Tribology*, 135 (4): 041502, 2013.

[21] O. O. Ajayi, C. Lorenzo-Martin, R. A. Erck, and G. R. Fenske. Scuffing mechanism of near-surface material during lubricated severe sliding contact. *Wear*, 271: 1750–1753, 2011.

[22] J. J. Liou. *A theoretical and experimental investigation of roller and gear scuffing*. PhD thesis, The Ohio State University, 2010.

[23] T. Nakatsuji and A. Mori. Tribological properties of electrolytically polished surfaces of carbon steel. *Tribology Transactions*, 41 (2): 179–188, 1998.

[24] W. T. Lai and H. S. Cheng. Temperature analysis in lubricated simple sliding rough contacts. *Tribology Transactions*, 28: 303–312, 1985.

[25] D. Zhu and Y. Z. Hu. A computer program package for the prediction of ehl and mixed lubrication characteristics, friction, subsurface stresses, and flash temperatures based on measured 3-d surface roughness. *Triology Transactions*, 44 (3): 383–390, 2001.

[26] J. Enthoven and H. A. Spikes. Infrared and visual study of the mechanisms of scuffing. *Tribology Transactions*, 39 (2): 441–447, 1996.

[27] K. Ichimaru, N. Izumi, M. Kimura, and K. Kobori. Effect of lubricant additives on scoring-proof capability of gear oils. *JSME International Journal, Series 3: Vibration, Control Engineering, Engineering for Industry*, 35 (4): 652–659, 1992.

[28] H. J. Kim, P. Ehret, D. Dowson, and C. M. Taylor. Thermal elastohydrodynamic analysis of circular contacts part 2: non-newtonian model. *Proc. Inst. Mech. Engrs., Part J: Journal of Engineering Tribology*, 215 (4): 353–362, 2001.

[29] H. Salehizadeh and N. Saka. Thermal non-newtonian elastohydrodynamic lubrication of line rolling contacts. *ASME Journal of Tribology*, 113 (3): 481–491, 1991.

[30] H. S. Hsiao and B. J. Hamrock. A complete solution for thermal elastohydrodynamic lubrication of line contacts using circular non-newtonian fluid model. *ASME Journal of Tribology*, 114 (3): 540–551, 1992.

[31] C. Hsu and R. Lee. An efficient algorithm for thermal elastohydrodynamic lubrication under rolling/sliding line contacts. *ASME Journal of Tribology*, 116 (4): 762–769, 1994.

[32] S. Li and U. Parmar. The effects of microdimple texture on the friction and thermal behavior of a point contact. *ASME Journal of Tribology*, 140: 041503, 2018.

[33] L. Qiu and H. S. Cheng. Temperature rise simulation of three-dimensional rough surface in mixed lubricated contact. *Journal of Tribology*, 120 (2): 310–318, 1998.

[34] C. Cioc, S. Cioc, L. Moraru, A. Kahraman, and T. G. Keith. A deterministic elasto-hydrodynamic lubrication model of high-speed rotorcraft transmission components. *Tribology Transactions*, 45 (4): 556–562, 2002.

[35] W. Z. Wang, Y. Z. Hu, Y. C. Liu, and H. Wang. Deterministic solutions and thermal analysis for mixed lubrication in point contacts. *Tribology International*, 40 (4): 687–693, 2007.

[36] N. Deolalikar, F. Sadeghi, and S. Marble. Numerical modeling of mixed lubrication and flash temperature in ehl elliptical contacts. *Journal of Tribology*, 130 (1): 011004, 2008.

[37] K. Yagi, K. Kyogoku, and T. Nakahara. Relationship between temperature distribution in ehl film and dimple formation. *ASME Journal of Tribology*, 127 (3): 658–665, 2005.

[38] T. Nakahara and K. Yagi. Influence of temperature distributions in ehl film on its thickness under high slip ratio conditions. *Tribology International*, 40 (4): 632–637, 2007.

[39] K. Yagi, K. Kyogoku, and T. Nakahara. Measurements of temperature distributions around longitudinally grooved rough surfaces in sliding elastohydrodynamic point contacts. *Tribology Transactions*, 49 (4): 482–489, 2006.

[40] B. J. Hamrock and D. Dowson. Isothermal elastohydrodynamic lubricaiton of point constants, part iv, starvation results. *Journal of Lubrication Tech.*, 99 (1): 15–23, 1977.

[41] F. Chevalier, A. A. Lubrecht, P. M. E. Cann, F. Colin, and Dalmaz G. Film thickness in starved ehl point contacts. *ASME Journal of Tribology*, 120 (1): 126–133, 1998.

[42] P. M. E. Cann, B. Damiens, and A. A. Lubrecht. The transition between fully flooded and starved regimes in ehl. *Tribology International*, 37 (10): 859–864, 2004.

[43] L. D. Wedeven, D. Evans, and A. C. Cameron. Optical analysis of ball bearing starvation. *ASME Journal of Lubrication Technology*, 93 (3): 349–361, 1971.

[44] P. Svoboda, D. Kostal, I. Kruptka, and M. Hartl. Experimental study of starved ehl contacts based on thickness of oil layer in the contact inlet. *Tribology International*, 67: 140–145, 2013.

[45] P. Yang, J. Wang, and M. Kaneta. Thermal and non-newtonian numerical analyses for starved ehl line contacts. *ASME Journal of Tribology*, 128 (2): 282–290, 2006.

[46] W. Pu, D. Zhu, and J. Wang. A starved mixed elastohydrodynamic lubrication model for the prediction of lubrication performance, friction, and flash temperature with arbitrary entrainment angle. *ASME Journal of Tribology*, 140 (3): 031501, 2018.

[47] M. Riggs, N. K. Murthy, and S. P. Berkebile. Scuffing resistance and starved lubrication behavior in helicopter gear contacts: dependence on material, surface finish, and novel lubricants. *Tribology Transactions*, 60 (5): 932–941, 2017.

[48] H. G. Elrod. A cavitation algorithm. *ASME Journal of Lubrication Technology*, 103 (3): 350–354, 1981.

[49] K. J. Johnson. *Contact Mechanics*. Cambridge University Press, 1985.

[50] B. J. Hamrock. *Fundamentals of Fluid Film Lubrication*. NASA Reference Publication 1255, 1991.

[51] J. A. Greenwood. Two-dimensional flow of a non-newtonian lubricant. *Proceedings of the Institution of Mechanical Engineers, Part J: Journal of Engineering Tribology*, 214 (1): 29–41, 2000.

[52] S. Bair and W. O. Winer. A new high-pressure, high-shear stress viscometer and results for lubricants. *Tribology Transactions*, 36 (4): 721–725, 1993.

[53] S. Bair. High-pressure rheology for quantitative elastohydrodynamics. *Elsevier Science*, Amsterdam, 2007.

[54] Y. Liu, Q. J. Wang, and S. Bair. A quantitative solution for the full shear-thinning ehl point contact problem including traction. *Tribology Letters*, 28 (2): 171–181, 2007.

[55] L. D. Wedeven and C. Cusano. Elastohydrodynamic film thickness measurements of artificially produced surface dents and grooves. *ASLE Transactions*, 22 (4): 369–381, 1979.

[56] K. Schmidt, S. Bair, and J. P. M. Trusler. The viscosity of squalane revisited - an updated reference model. *16^{th} Meeting of the International Association for Transport Properties*, July 15 2016, Imperial College London, U.K.

[57] S. Bair. *High Pressure Rheology for Quantitative Elastohydrodynamics*. Elsevier, Amsterdam, Netherlands, 2019.

[58] S. Li and A. Kahraman. A mixed ehl model with asymmetric integrated control volume discretization. *Tribology International*, 42 (8): 1163–1172, 2009.

[59] S. Li and A. Kahraman. Prediction of spur gear mechanical power losses using a transient elastohydrodynamic lubrication model. *Tribology Transactions*, 53 (4): 554–563, 2010.

[60] S. Li and A. Anisetti. On the flash temperature of gear contact under the tribo-dynamic condition. *Tribology International*, 97: 6–13, 2016.

[61] S. Li and A. Anisetti. A tribo-dynamic contact fatigue model for spur gear pairs. *International Journal of Fatigue*, 98: 81–91, 2017.

[62] S. Li, A. Kahraman, and M. Klein. A fatigue model for spur gear contacts operating under mixed elastohydrodynamic lubrication conditions. *Journal of Mechanical Design*, 134 (4): 041007, 2012.

[63] K. H. Kim and F. Sadeghi. Three-dimensional temperature distribution in ehd lubrication. part i: circular contact. *ASME Journal of Tribology*, 114 (1): 32–41, 1992.

[64] H. S. Carslaw and J. C. Jaeger. *Conduction of heat in solids*. Oxford Press, 1959.

[65] S. Li. Influence of surface roughness lay directionality on scuffing failure on lubricated point contacts. *ASME Journal of Tribology*, 135 (4): 041502, 2013.

[66] E. Querlioz, F. Ville, and T. Lubrecht. Experimental investigations on the contact fatigue life under starved conditions. *Tribology International*, 40 (10-12): 1619–1626, 2007.